Crumpled Polymer with Loops Recapitulates Key Features of Chromosome Organization

Kirill E. Polovnikov,[1,*] Hugo B. Brandão,[2] Sergey Belan,[3,4] Bogdan Slavov,[1] Maxim Imakaev,[5] and Leonid A. Mirny[5,6,†]

[1]*Independent Researcher, Moscow, Russia*
[2]*Illumina Inc., 5200 Illumina Way, San Diego, California 92122, USA*
[3]*Landau Institute for Theoretical Physics, Russian Academy of Sciences, Chernogolovka, Russia*
[4]*National Research University Higher School of Economics, Faculty of Physics, Moscow, Russia*
[5]*Institute of Medical Engineering and Science, Massachusetts Institute of Technology, Cambridge, Massachusetts 02139, USA*
[6]*Department of Physics, Massachusetts Institute of Technology, Cambridge, Massachusetts 02139, USA*

(Received 2 May 2023; accepted 4 August 2023; published 13 November 2023)

Chromosomes are exceedingly long topologically constrained polymers compacted in a cell nucleus. We recently suggested that chromosomes are organized into loops by an active process of loop extrusion. Yet loops remain elusive to direct observations in living cells; detection and characterization of myriads of such loops is a major challenge. The lack of a tractable physical model of a polymer folded into loops limits our ability to interpret experimental data and detect loops. Here, we introduce a new physical model—a polymer folded into a sequence of loops—and solve it analytically. Our model and a simple geometrical argument show how loops affect the statistics of contacts in a polymer across different scales, explaining universally observed shapes of the contact probability. Moreover, we reveal that folding into loops reduces the density of topological entanglements, a novel phenomenon we refer to as "the dilution of entanglements." Supported by simulations, this finding suggests that up to approximately 1–2-Mb chromosomes with loops are not topologically constrained, yet become crumpled at larger scales. Our theoretical framework allows inference of loop characteristics, draws a new picture of chromosome organization, and shows how folding into loops affects topological properties of crumpled polymers.

DOI: 10.1103/PhysRevX.13.041029

Subject Areas: Biological Physics, Soft Matter, Statistical Physics

I. INTRODUCTION

Three-dimensional organization of chromosomes is a multiscale complex physical system that has been challenging the field of polymer physics and stimulated the development of a broad range of polymer models. Such models mostly concern large-scale properties of chromosomes and include topologically constrained polymers [1–4], nonequilibrium polymer states [5,6], gels and supercoiled polymers [7], and active polymers systems [8,9].

Recent experiments allowed characterizing chromosome folding at all scales. A Hi-C experiment produces a map of contact frequency $P(i,j)$ between all pairs of genomic positions i and j [10]. In addition to a variety of local features visible in $P(i,j)$ maps [11], the physical state of a chromosome polymer can be characterized by the scaling of the average contact probability $P(s)$ with the genomic distance $s = |i-j|$. At large scales, in the range of $s = 1$–5 Mb, the scaling of $P(s) \sim s^{-1}$, markedly different from $s^{-3/2}$ expected for an ideal chain [i.e., 3D random walk with segment size $R(s) \sim s^{1/2}$] or approximately $s^{-3/2}$ followed by a plateau for the equilibrium globule [12]. The $P(s) \sim s^{-1}$ scaling suggested that chromosomes are folded into the "crumpled" states [1,10,13] conjectured more than three decades ago [14,15]. These polymer states are characterized by largely unknotted conformations that are stabilized by topological interactions between segments of the chain, i.e., their inability to cross each other. A chain from the melt of large unknotted nonconcatenated rings is a canonical example of the topologically stabilized polymer state, which is believed to have the fractal dimension $d_f = 3$ asymptotically [$R(s) \sim s^{1/d_f}$ and $P(s) \sim s^{-\gamma}, \gamma \approx -1.1$] [1,3,16–18] at scales $s \gg N_e$, where N_e is the entanglement length. As we show below, the existence of the minimal scale (the topological blob), at which the crumpled polymer actually develops the crumpled statistics has a crucial impact on the organization of chromosomes.

*Corresponding author: kipolovnikov@gmail.com
†Corresponding author: leonid@mit.edu

At smaller scales, the $P(s)$ curve generally exhibits not a power-law behavior with a characteristic "shoulder" at $s \approx 100$–200 kb, which, as we show below, reflects folding of the chain into loops. We and others suggested that at smaller scales ($s < 1$ Mb), chromosomes are folded into loops formed by an active, energy-dependent process of loop extrusion. We hypothesized that loop-extruding motors associate with a chromosome, extrude loops, and dissociate, thus maintaining the chromosome polymer in the steady state, where it is folded in an array of nonoverlapping randomly positioned loops [19,20]. Loop extrusion was observed *in vitro* [21], yet detecting and characterizing myriads of transient loops presumably present *in vivo* remains a major challenge.

Other models of interphase chromosomes folded into different types of loops, including giant rings (3–4 Mb) [22], random overlapping loops (cross-links) with a broad size distribution [23,24], and rosettes of loops [25], were proposed but not systematically tested against Hi-C data. An analytical solution for even the simplest case of random cross-links [26], however, gave $P(s) \sim s^{-3/2}$ followed by a plateau being markedly different from the experimental $P(s)$. Dense arrays of loops were also considered in models of mitotic chromosomes [27], where the interplay of factors determine the "optimal-sized" loops that maximize compaction and simultaneously minimize interchromosome entanglements. While accumulation of experimental data about interphase chromosomes continues yielding $P(s)$ curves of similar shapes, no polymer physics model was used to address such a universal $P(s)$ and to qualitatively characterize the organization of chromosomes.

The main challenge for an overarching model of chromosome organization is to take into account both the crumpled statistics of the chain and its folding into loops. While some attempts have been made to explain the crumpled organization itself by loops (e.g., Refs. [24,28,29]), recent experiments have clearly demonstrated that they represent two independent modes of chromatin organization. Experimental depletion of a loop-extruding protein complex of cohesin has removed the local shoulder on $P(s)$ at $s < 1$ Mb and revealed the power-law behavior of $P(s) \sim s^{-1}$ in the 2 orders of magnitude range of scales $s \approx 50$–5000 kb [30,31].

Here we develop a model of a polymer of an arbitrary fractal dimension d_f (including $d_f = 3$ for the crumpled state) folded into randomly positioned and nonoverlapping loops, as expected to be produced out of extrusion. Our model being analytically tractable shows how such loops perturb fractal polymer organization across scales, agrees with a broad range of experimental Hi-C data, and allows us to infer parameters of the loops organization. Furthermore, we reveal and describe a novel topological phenomenon, the dilution of entanglements, taking place in a crumpled chain folded into short-scale unentangled loops. Namely, we demonstrate that the loops drastically increase the entanglement length N_e of a crumpled chromosome backbone (approximately tenfold or even more).

We suggest that at megabase length scales, a chromosome resembles a comblike polymer with an ideal backbone and short unentangled loops. Our study provides a novel view of the organization of chromosomes and, broadly, of topologically stabilized polymer chains, where density of topological constraints can be modulated by formation of short-scale loops.

II. A MODEL: POLYMER CHAIN FOLDED INTO LOOPS

Let us consider a classical bead-spring model of a polymer chain [12,32,33]. Without long-ranged interactions it corresponds to a three-dimensional random walk at sufficiently large scales (i.e., ideal chain with fractal dimension $d_f = 2$). One can generalize it to the case of arbitrary fractal dimension $d_f \geq 2$ via introduction of special quadratic pairwise interactions between the beads [2], in particular, allowing us to describe the crumpled states with $d_f = 3$. The effective interactions result in the mean-squared spatial size of the polymer segment of s beads that behaves as $r^2(s) \sim s^{2/d_f} b^2$ for beads of the length b. An important experimentally measured characteristic of such a chain is the contact probability between ends of the segment $P_0(s)$ that according to the mean-field argument [1,10,18,34] is inversely proportional to the volume spanned by the segment

$$P_0(s) \propto \frac{1}{s^{3/d_f}}. \tag{1}$$

Though Eq. (1) is not true in general, it holds for the class of fractional Brownian polymers [2,4,35], for which Eq. (1) is the normalization of the Gaussian distribution of end-to-end distance.

Now, we consider this fractal chain folded into consecutive and nonintersecting loops with the average contour length λ and separated by gaps that have an average contour length g both exponentially distributed [Fig. 1(a)]. Importantly, we assume that the fractal dimension d_f of the polymer at large scales and within a loop is not changed by the addition of the loops. Also, each "loop" is modeled as an additional bond in its base, so that the ring-shaped cohesin protein does not topologically embrace two strands of chromatin but chemically binds them [36]. Then the full sequence of the gaps comprises the main chain (the backbone), controlling its equilibrium conformation properties at large scales. Clearly, such folding into loops reduces distances in polymer, turning it into a comblike chain with loopy side bristles.

The effect of the loops on $P(s)$ can be calculated using the frozen disorder approach as follows. First, one classifies possible positions of the two points i, j with respect to the loop bases [four different "diagrams," Fig. 2(a)] and then

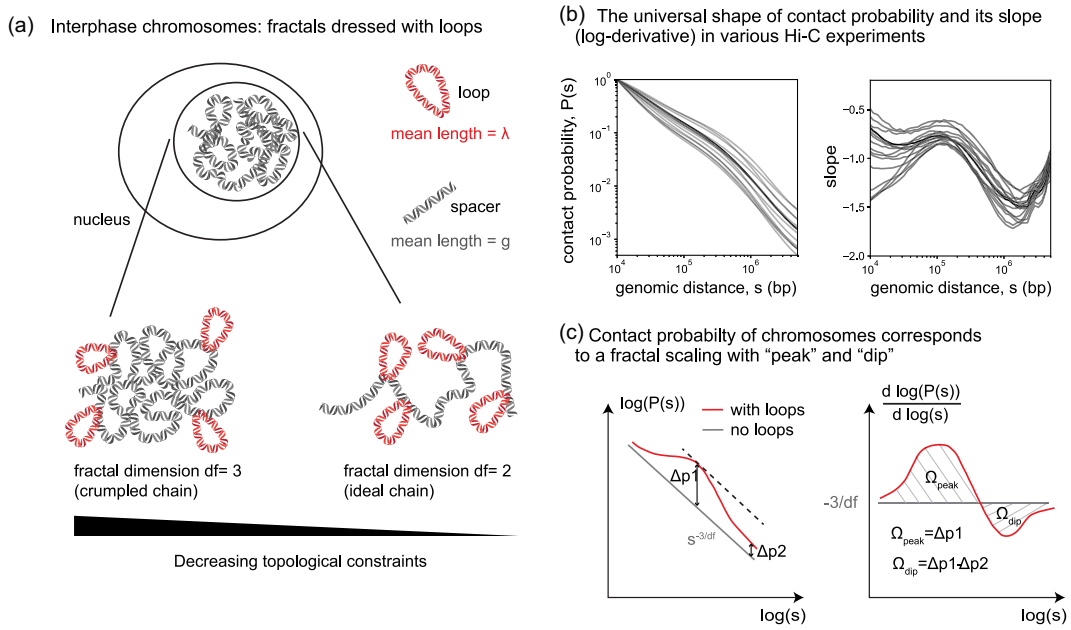

FIG. 1. Folding of a fractal polymer into random loops recapitulates universal $P(s)$ profiles in Hi-C experiments. (a) A sketch of fractal polymers with different fractal dimensions d_f folded into loops. The mean size of the loops is λ, the mean size of the gaps (spacers) is g. (b) A collection of 24 contact probability curves $P(s)$ (left) and its log-derivatives (right) from experimental Hi-C and Micro-C data for different human cell types [37–39]. The shape of the profiles is universal across experimental conditions and cell types. (c) A sketch of the typical behavior of the contact probability $P(s)$ with and without loops (left) along with its logarithmic derivative (right) up to several megabases. A geometrical argument explains that formation of the dip is due to the difference in elevation of $P(s)$ at small and large scales.

calculates the contact probability in each case at equilibrium. For each diagram, one computes the variance $\langle r^2 \rangle$ of the vector $\vec{r}$ connecting the points of interest and makes use of the Gaussian relation $P(s) \sim \langle r(s)^2 \rangle^{-3/2}$ for the corresponding equilibrium contact probability; see Eq. (1). For Fig. 2(a) diagrams **b** and **d**, the vector $\vec{r}$ is decomposed into the sum of independent vectors $\vec{r}_1$ (loop), $\vec{r}_2$ (backbone) and $\vec{r}_1$ (loop), $\vec{r}_2$ (backbone), $\vec{r}_3$ (loop), respectively. In Fig. 2(a) diagrams **b**–**d**, a loop resembles a fractal bridge of the same dimension d_f, for which the effective Hamiltonian from Ref. [2] is used (see Appendix A).

Second, one averages these probabilities over all possible pairs of monomers i, j involving different diagrams, such that $|i - j| = s$ [Fig. 2(a)]. The exponential distribution of lengths for loops and gaps allows us to make use of the well-known expression for the propagators of the two-state Markov process [41] and properly weigh contributions of different diagrams. Finally, the remaining averaging over the distribution of random loops and gaps is performed (see Appendix A). The ultimate result is factorized into the unconstrained conditional probability $P_0(s)$ of a loop-free chain Eq. (1) and function $\mathcal{P}$ of the scaled genomic distance s/λ and the fraction parameter $d = \lambda/g$ (for connection of this parameter to the linear loop fraction, see Ref. [42]):

$$P(s)/P_0(s) = \mathcal{P}(s/\lambda; \lambda/g). \tag{2}$$

The function $\mathcal{P}$ accurately accounts the contributions from four diagrams [Fig. 2(a) diagrams **a**–**d**]; it is expressed in the form of multiple integrals involving the Bessel functions, which are to be computed numerically.

Strikingly, already for the ideal chain ($d_f = 2$) folded into loops the shape of the $P(s)$ curve, best represented by its log-derivative $d \log P(s)/d \log(s)$, qualitatively matches the corresponding curves computed from experimental Hi-C data; see Figs. 2(b), 2(c), and 1(b).

In accord with experiments [Fig. 2(c)], loops perturb the power-law behavior of the $P(s)$ curve and result in the formation of a shoulder at $s \approx \lambda$, and a corresponding "peak" and "dip" on the log-derivative plot; see Fig. 1(c). Moreover, in line with our theory, experiments where loops are eliminated by depletion of cohesin (a loop-extruding motor) [30,31] give $P(s)$ with an almost constant slope (i.e., fractal) from approximately 50 to 5000 kb, yielding a near constant in the log-derivative without the characteristic peak and the dip [see Fig. 2(c), left]. Furthermore, experiments where loop sizes were increased by depleting the protein Wapl [see Fig. 2(c), right] demonstrate an extension of the $P(s)$ shoulder and displacement of the peak on the log-derivative on the right. Consistently, we see that in our model [Fig. 2(b)] the shoulder on $P(s)$ and the peak on the log-derivative curve travel to the right upon the increase of the mean loop length λ at fixed λ/g (for other effects in WaplKO, see Sec. III.).

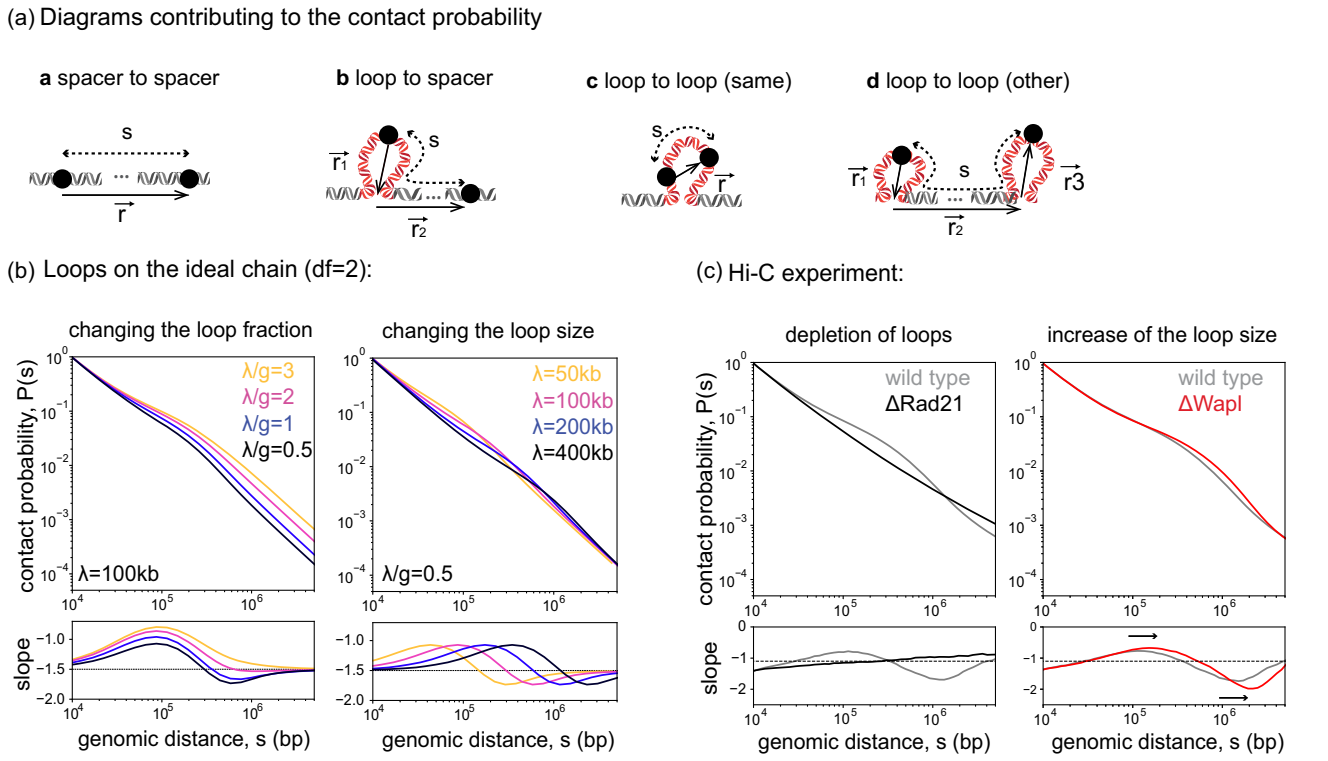

FIG. 2. Contact probability for the fractal chain folded into an array of random loops. (a) Illustration of the possible diagrams contributing to the contact probability. The three dots (…) denote a chromosome segment that may contain an arbitrary number of loops. (b) Evolution of the $P(s)$ and its log-derivative for the ideal chain ($d_f = 2$) upon the change of the parameter $d = \lambda/g$ (left) and the mean loop length, λ (right), where the value of the other parameter is fixed as indicated. (c) Behavior of the $P(s)$ and its log-derivative in a Hi-C (specifically, Micro-C) experiment upon (left) disruption of cohesin complexes by Rad21 depletion, thus eliminating loops. Right: Wapl depletion, thus increasing the loops size (loop fraction also increases in WaplKO turning a chromosome into a dense bottle brush [40]; see Sec. III). Rad21 is a subunit of cohesin; thus, its near-complete depletion results in disruption of cohesin-mediated loops on chromosomes. Wapl protein, on the contrary, unloads cohesin from chromosomes; thus, its depletion increases cohesin residence time and, as a result, the average loop length λ. The cell type is mouse embryonic stem cell; same for the two datasets [30].

As we see, using the simplest prior (ideal chain, $d_f = 2$) it is possible to explain qualitatively how the loops change the shape of the log-derivative. However, the ideal chain model does not capture an important aspect of chromosome organization such as the value of the $P(s)$ slope closer to -1, rather than $-3/2$ in most cell types [1,10,13–16]. Indeed, the scaling of approximately -1 stretches for 2 orders of magnitude in genomic scale s, when cohesin-mediated loops are eliminated [30,31,43] [Fig. 2(c)]. According to Eq. (1), it corresponds to the almost compact fractal folding with $d_f \approx 3$. Such characteristics are features of the crumpled folding of a polymer, e.g., in a equilibrium melt of nonconcatenated unknotted rings [1,3,13,16–18] or as a long-lived nonequilibrium state of a collapsed linear chain [5,6,14].

The results for a nonideal polymer with $d_f > 2$ are shown in Fig. 3(a) and Supplemental Material Fig. S1 [44]. In particular, the loopy chain folded with a larger fractal dimension has a slower decaying $P(s)$ than the ideal chain with $d_f = 2$ at all scales, the former being consistent with Hi-C data. Accordingly, the baseline (loop-free) slope of $P(s)$, i.e., its asymptotic value $[d\log P_0(s)/d\log s] = -3/d_f$, is lifting up with increase of d_f. These properties are not surprising, since they are put in the model by construction. A nontrivial observation, however, is that the amplitudes of peak and dip on the log-derivatives notably diminish for a nonideal chain [Fig. 3(a) and Supplemental Material Fig. S1 [44]). Intuitively, this can be rationalized, as additional compactness by means of loops has a weaker effect on already somewhat compact chains with $d_f > 2$. In other words, formation of loop constraints on more compact chains requires more subtle rearrangement of the particles in space and leads to weaker perturbation of the contact statistics.

To additionally validate our analytical computations we compare them to numerical simulations. To calculate the contact probability $P(s)$, (i) the loci i, j at the given contour distance $s = |i - j|$ are sampled on the randomly generated sequences of exponentially distributed loops and gaps, (ii) the mean equilibrium distances between the loci are computed according to the diagram they belong to, (iii) the distances are translated into the contact probabilities using

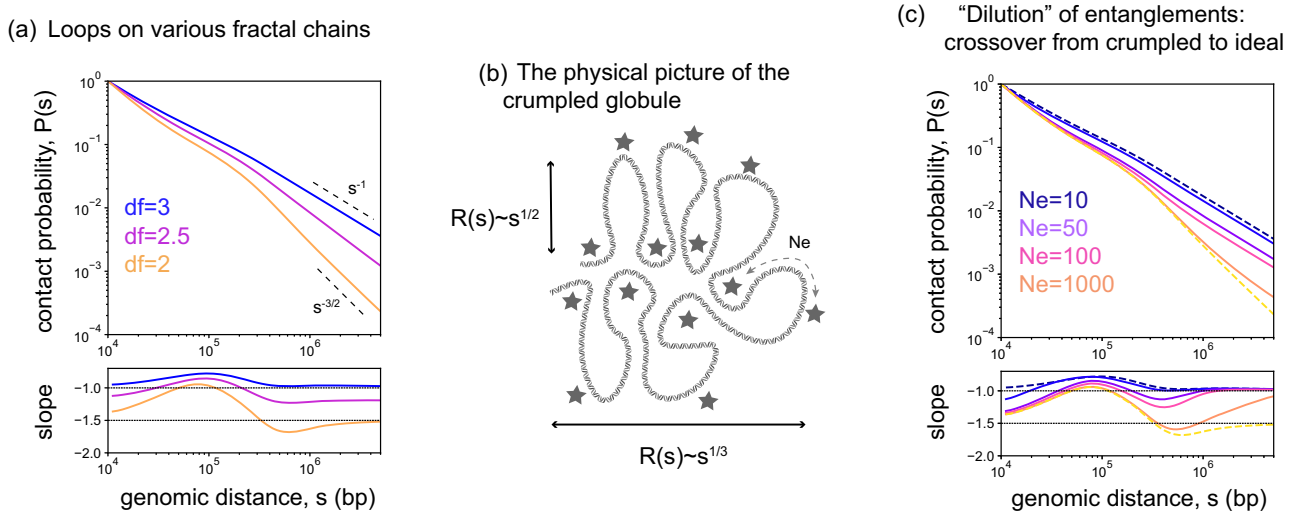

FIG. 3. Effects in the nonideal chain: a polymer with $d_f > 2$ folded into loops. (a) The effect of the fractal dimension on $P(s)$ and its log-derivative ($\lambda/g = 1, \lambda = 100$ kb). (b) A physical picture of the crumpled polymer as a chain in the space with topological obstacles [45]: At short scales (between the obstacles) it is ideal ($d_f = 2$) and at large scales it is crumpled ($d_f = 3$). The entanglement length N_e defines a crossover length scale between the two regimes. (c) Upon the increase of N_e a crumpled polymer restores ideal statistics at larger length scales ($\lambda/g = 1, \lambda = 100$ kb). The dash curves respond to asymptotic loopy fractals with $N_e = 0$ ($d_f = 3$, blue) and $N_e = \infty$ ($d_f = 2$, yellow). N_e is measured in kb.

the mean-field relation Eq. (1) and, finally, (iv) the sample averaging is performed. This approach essentially allows us to weight the contributions of different diagrams numerically via statistical sampling, while keeping the end-to-end distribution Gaussian. As we demonstrate in the Fig. S3 in the Supplemental Material [44], the numerical approach perfectly agrees with the results of our theory, irrespective of the value of λ/g.

A simple argument helps us to understand how loops perturb the contact probability $P(s)$ generating the curves we observe in the theory and experiments [Fig. 1(c)]. Indeed, the loops impose two effects on $P(s)$ at different scales. At small scales, the dominant contribution to the elevation of $P(s)$ comes mainly from contacts between two loci within the same loop (e.g., see Supplemental Material Fig. S2 [44] for $\lambda/g \geq 1/5$). Within a loop, the contact probability is increased due to the smaller physical size of a loop compared to an open chain of the same contour length, and due to a shorter effective contour length between two points near the loop base. Thus,

$$P(s)/P_0(s) \approx 1 + \Omega(s/\lambda)\frac{\lambda}{\lambda + g}; \qquad s \leq \lambda, \tag{3}$$

where $\Omega(s/\lambda)$ is some function describing the shape of the shoulder, which is weighted by the fraction of the chain within the loops.

At large scales, when $s \gg \lambda$, the contact probability becomes elevated due to a shorter effective contour length between the two points, since the shortest path between monomers skips all intervening loops:

$$P(s)/P_0(s) \propto \left(\frac{\lambda}{g} + 1\right)^{3/d_f}; \qquad s \gg \lambda. \tag{4}$$

The interplay between the shoulder at small scales Eq. (3) and the elevation of $P(s)$ at large scales Eq. (4) determines the shape of $P(s)$ as well as the peak and the dip of the log-derivative. The peak is always present as a result of breaking of the scale invariance due to loops formation. Figure 1(c) displays a simple geometric condition for the dip: The shoulder Eq. (3) at $s \approx \lambda$ must be higher than the elevation at $s \gg \lambda$ Eq. (4). As the spacer g shrinks (loop fraction increases), the elevation at large scales Eq. (4) indefinitely grows, while the height of the shoulder Eq. (3) eventually saturates. Therefore, upon a gradual compaction of the chain into an array of loops, the dip becomes more shallow and dissolves. As the solution for the ideal chain ($d_f = 2$) suggests [Fig. 2(b) left and Supplemental Material Fig. S1 [44]), there is a critical value of parameter $d = (\lambda/g)^* \approx 2$, at which the dip completely disappears. For the compact chain ($d_f = 3$), the corresponding critical values are lower, $d = (\lambda/g)^* \approx 1$. Indeed, since the absolute perturbation at the shoulder $\Omega(s/\lambda)$ is smaller for chains with $d_f > 2$, the dip disappears at a lower loop fraction than for the ideal chain. Physically, this marks a crossover from sparse to relatively dense array of loops where the effective shortening of the polymer at large scales reaches the level of compaction at scales of a single loop.

A. Loops on a crumpled chain

The crumpled statistics cannot be realized at all scales in a physical system [3,14,16,17]. For a physical crumpled

chain, there is a crossover length scale N_e called the entanglement length (having the meaning of the topological blob), only above which the compact folding with $d_f = 3$ can take place. Below this scale, the topological constraints are not sufficient, and the segment remains ideal with $d_f = 2$ down to the persistent length (for a loosely entangled chain) or the concentration blob size [12,32]. The end-to-end squared size of a segment s of a crumpled chain with the entanglement length N_e and the persistent length l_p can be written as

$$r^2(s) = \begin{cases} s l_p b^2 & \text{for } l_p < s \le N_e, \\ s^{2/3} N_e^{1/3} l_p b^2 & \text{for } s \ge N_e. \end{cases} \tag{5}$$

To quantitatively explore the effect of this crossover in real crumpled chains on $P(s)$, we generalize our theory to a nonfractal chain governed by Eq. (5). For smoothness of resulting $P(s)$, we allow the crossover point in Eq. (5) to fluctuate around the mean N_e with the exponential distribution (see Appendix A 6).

We find that considering the scale N_e, where topological effects start to play an important role, changes the behavior of the $P(s)$ in the model. With increasing N_e, the crumpled polymer with loops starts to show a much more pronounced dip on the log-derivative curve [Fig. 3(c)]. Since for $s < N_e$ the system behaves like an ideal chain with loops, for $N_e \gg \lambda$ the effect of topological crumpling becomes irrelevant, and the log-derivative curve resembles that of loops on an ideal chain. Figure 3(c) demonstrates this crossover from the crumpled (blue) to ideal chain regimes (yellow), upon the increase of N_e, with a pronounced "peak and dip" emerging when $N_e \approx \lambda$. For example, for $\lambda/g = 1$ and $N_e = 50 \sim \lambda = 100$ kb, not atypical for dense polymer systems, one has a pronounced dip on the log-derivative, which is otherwise absent in the model without N_e. Further increase in N_e results in an even deeper dip, while the amplitude of the peak located at approximately λ saturates.

The pronounced dip requires $N_e \gtrsim \lambda$, which in turn indicates that extruded loops cannot be crumpled. For a ring to be crumpled it needs to be several dozens of N_e in length (10–30N_e) [18,46]. At the same time, the entanglement length for chromatin estimated in the literature (see Table 2 in Ref. [1]; $N_e \approx 20$–100 kb) is comparable to the size of cohesin-mediated loops $\lambda \approx 100$–150 kb. Therefore, this picture suggests that the extruded loops in chromatin are practically not crumpled (unentangled).

Remarkably, a crumpled chain with unentangled loops captures both the pronounced peak and dip and leveling of the curve at approximately -1 both seen across Hi-C experiments [see Fig. 1(b)], and not captured by models that we considered above (the ideal chain and the fractal chains with $d_f > 2$).

B. Dilution of entanglements in a crumpled chain induced by folding into loops

Can folding into unentangled loops, in turn, affect entanglements of the main chain? In what follows, we suggest that since the loops are unentangled they do not impose any considerable topological constraints for the main chain. As more material goes into loops, the main chain shortens, which leads to the decrease of the total amount of entanglements (dilution) and increase of N_e of the main chain. This effect that we refer to as the "dilution of entanglements" can be physically understood as the screening of entanglements by the loops inside the growing topological blob. As we demonstrate below, N_e of the main chain indeed grows with the loop fraction, which in turn affects the contact probability $P(s)$ of the loopy chain across scales. This way, the effects of the large N_e considered in the previous section become even stronger.

To estimate the effect of loops on N_e of the main chain, we start with a known empirical expression for dense linear chains [1,47,48]:

$$N_e = l_k \left(\left(\frac{1}{c_\xi \varphi_k} \right)^{2/5} + \left(\frac{1}{c_\xi \varphi_k} \right)^2 \right), \tag{6}$$

where l_k is the Kuhn length (in monomers), $\varphi_k = \varphi v_k / l_k = \varphi l_k^2$ is the dimensionless volume density of Kuhn segments of volume v_k, and monomer volume density φ; $c_\xi \approx 0.06$ is a phenomenological constant that is used to describe various simulation data for entangled polymers [47]. For loosely entangled linear chains $\varphi_k < 1$, the quadratic factor in Eq. (6) dominates. Furthermore, for crumpled territorial chains described by Eq. (5), one can show that the Kuhn volume density of a single chain is similarly related to its entanglement length,

$$N_e = l_k \left(\frac{M}{\varphi_k} \right)^2 \tag{7}$$

for all φ_k and where $M \sim 1$ is the number of territorial chains overlapping with each other (the overlap parameter [32]). The dependence of N_e on φ_k for the crumpled polymer can be understood in the picture of a chain in the array of topological obstacles (constraints) [49,50], which is collectively generated by spatial contacts between the crumples [see Figs. 3(b) and 4(a)]. Clearly, not all spatial contacts contribute to topological obstacles. However, similar to linear chains [48], nonspecific dilution of the contacts upon decrease of φ_k leads to fewer topological obstacles in the system and, accordingly, increases the entanglement length N_e Eq. (7).

We suggest that due to the commutative relation between topological obstacles (if a segment A creates an obstacle for a segment B, then segment B creates an obstacle for segment A), unentangled loops do not produce topological obstacles and hence do not crumple the main chain.

Thus, in our system the effective volume density φ_k^{eff} relevant for the entanglements is controlled by the backbone, which is shortening upon folding into loops. Still, the loops occupy a certain excluded volume in the space, creating the crowding effect for the main chain. The two phenomena, backbone shortening and loops crowding, are encoded in the theory for φ_k^{eff} of a crumpled polymer folded into loops of size λ and loop fraction parameter $d = \lambda/g$ (see the accurate derivation in Appendix B):

$$\varphi_k^{\text{eff}} = \frac{\varphi_k^{(0)}}{1 + d(1 - c_\alpha \varphi_k^{(0)} \lambda^{1/2})}; \qquad N_e = N_e(\varphi_k^{\text{eff}}), \tag{8}$$

where the constant c_α depends on the microscopic structure of the fiber $c_\alpha \propto l_k^{-1/2}$; we treat c_α as a free parameter in our model. The structure of Eq. (8) can be understood as follows. Without loops ($d = 0$), the backbone resembles the original crumpled chain with effective volume density $\varphi_k^{(0)}$. If the loops are sufficiently short so that their volume can be neglected, the decreased effective volume density is fully described by the backbone shortening, which yields the factor $d + 1 = (\lambda + g)g^{-1}$ in the denominator of Eq. (8). In general, the loops partially compensate this effect by crowding the own volume of the chain, which leads to an increase of φ_k^{eff}. Importantly, as we show in Appendix B, the compensation by the loops is always not complete ($c_\alpha \varphi_k^{(0)} \lambda^{1/2} < 1$) for unentangled loops.

The effect of dilution of entanglements Eq. (6)–(8) on $P(s)$ can be well captured by extending our analytical framework (the full theory). For that, we consider ideal loops, while the entanglement length N_e of the crumpled backbone is now a certain function of loop size and loop fraction, $N_e = N_e(\varphi_k^{\text{eff}}(\lambda, \lambda/g))$. Qualitatively, the effect on $P(s)$ can be understood as follows. As previously, the shape of $P(s)$ at scales $s \approx \lambda$ Eq. (3) is largely determined by intraloop contacts and is not sensitive to organization of the backbone chain. However, at large scales $s \gg \lambda$ the contact probability is now additionally decreased by the factor of $N_e^{1/2}$, reflecting spatial segregation of the loops due to the dilution of entanglements of the main chain

$$P(s)/P_0(s) \propto \frac{d+1}{\sqrt{N_e(d)}}, \qquad s \gg \lambda. \tag{9}$$

As we see from Eq. (9), the increase in contact frequency due to chain shortening is now counteracted by spatial separation of the loops due to the increased N_e [Fig. 4(a)]. Since in the regime of interest the entanglement length quadratically depends on the loop fraction parameter d, as seen from Eqs. (7) and (8), at $s \gg \lambda$ one has

$$P(s)/P_0(s) \propto \frac{d+1}{\alpha d + 1}, \qquad \alpha = 1 - c_\alpha \varphi_k^{(0)} \lambda^{1/2}. \tag{10}$$

Interestingly, for sufficiently short unentangled loops $\alpha \approx 1$, the backbone decompaction almost fully compensates its shortening [the crowding of loops, i.e., $\alpha < 1$, still slightly elevated $P(s)$ at small d]; see Fig. 5(a) and Supplemental Material Fig. S8 [44]. This result is physically related to the territorial organization of crumpled chains. Indeed, the size of the crumpled chain is controlled by the combination $NN_e^{1/2}$ [see Eq. (5)]; shortening of the backbone due to loops by a factor $d + 1$ leads to increase of $N_e^{1/2}$ by the same factor. As a result, crumpled chains with short-scale loops tend to decompact their shortened backbones to the volume of their own territories, nearly maintaining the spatial organization at large scales. While at large scales $P(s)$ is almost unchanged [$\Delta p_2 = 0$ in Fig. 1(c)], at short scales it is elevated due to folding into loops ($\Delta p_1 > 0$) [see Eq. (3)], which ensures formation of the dip independent of the loop fraction [Fig. 5(a)]. Thus, territoriality of crumpled chains underlies the observed universality of experimental $P(s)$ curves [Fig. 1(b)].

Taken together, the phenomenon of dilution of entanglements in real crumpled chains results in significant increase of N_e of the main chain upon folding of a polymer into loops. This effect in turn restores the dip on the log-derivative compared to the model with fixed N_e, and generates the universal shapes of the contact probability observed experimentally.

1. Simulations of crumpled chains with loops

Next we examine the dilution of entanglements by direct polymer simulations. To test predictions of the theoretical argument above, we perform equilibrium polymer simulations of a crumpled loopy polymer rings ($N = 90\,000$ beads, approximately equal to 90-Mb chromosomal region) with excluded volume and topological constraints (see Appendix C).

We observe that despite topological constraints, and consistent with the theory, the loops on the chains are indeed ideal, as their squared gyration size $R_g^2(L)$ grows linearly with their contour length L; Fig. 4(c).

Furthermore, we observe the increase of entanglement length N_e of the backbone with $d = \lambda/g$. In order to accurately check for this effect, we infer N_e and l_p by fitting $R(s)$ of the backbones from simulations by a theoretical curve. This curve is constructed by extending the wormlike chain model [51] to take into account the crossover from ideal to crumpled statistics at N_e (see Appendix C for details). Importantly, while the persistence length of the chain remains unchanged ($l_p = 1.75$) as a result of the addition of loops, we see that the entanglement length grows sixfold from $N_e \approx 70$ kb at $d = 0$ to $N_e \approx 420$ kb at $d = 3$ (Supplemental Material Fig. S4 [44]). As we find, the values of the entanglement length of the backbone directly measured in simulations are in excellent agreement with our theoretical predictions by Eqs. (6) and (8); see Fig. 4(b).

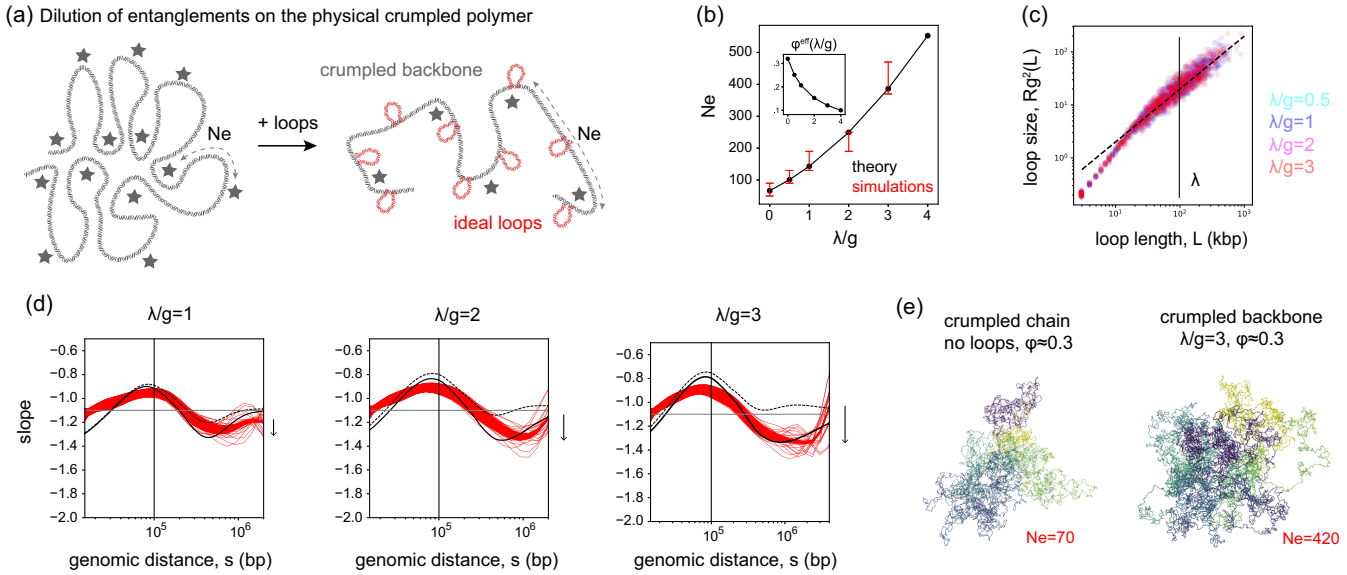

FIG. 4. Dilution of entanglements upon folding of a crumpled chain into loops. (a) A sketch of the effect of dilution of entanglements upon addition of the loops. Short-scale loops are unentangled and do not contribute to the crumpling of the backbone. Shortening of the backbone of the chain with loops (right) as compared to the loopsless situation (left) drives reduction of entanglements and increase of N_e. (b) Increase of the entanglement length N_e (in kb) as a function of parameter $d = \lambda/g$ as measured in simulations (red) and computed in the theory according to Eq. (6)–(8) (black). For the theoretical curve, the conventional value of the parameter $c_\xi = 0.06$ in Eq. (6) is used, which was previously found in Ref. [47] to match various entangled systems; the value of the microscopic constant c_α in Eq. (8) is found to be $c_\alpha \approx 0.02 l_k^{-1/2}$, which yields $c_\alpha \approx 0.01$ for $l_k \approx 4$ kb. The corresponding decrease of the effective monomer volume density φ^{eff} [which is l_k^2 times smaller than φ_k^{eff} in Eq. (8)] is shown in the inset. (c) Squared gyration size of the loops in simulations as functions of their contour length for various loop fractions, measured in σ^2, where σ is the size of a 1-kb monomer (approximately equal to 20 nm). The average loop size is $\lambda = 100$ kb. The dashed line is $R_g^2(L) \sim L$ shown for reference. (d) Slopes of the contact probability $P(s)$ for various loop fractions $\lambda/g = 1$, 2 and $\lambda/g = 3$ from simulations (red); theory with fixed $N_e = N_e(\lambda/g = 0) = 70$ kb (dashed black); theory with $N_e(\lambda/g)$ that is growing with the loop fraction, according to (b) (solid black). The value $d_f = 2.7$ (not $d_f = 3$) is chosen for the theory as it corresponds to the loop-free slope $3/d_f \approx 1.1$ in simulations (not -1). The red strip of the simulations is bound by two values of cutoff (capture radius of contact): $r_c = 3\sigma$ and $r_c = 5\sigma$. Different thin red lines correspond to different replicates. The average loop size is indicated by the vertical line $\lambda = 100$ kb. The arrow indicates deepening of the dip in the theory upon taking into account the dilution of entanglements. (e) The snapshots from simulations are shown for the backbone of a chain with loops ($\lambda/g = 3$, right) and for the main chain with cut and removed loops and further confined to the original monomer volume density $\varphi \approx 0.3$ (left).

Next we examine the physical origin of the backbone decompaction, i.e., the growth of N_e. The theory suggests that this effect is due to dilution of entanglements, and not due to the extension of the backbone by repulsion between the loops. To test this, we run additional simulations where we cut off loops from the backbone, turning it into the system of disconnected loops and the backbone. Then, we equilibrate the resulting system under the same total volume density. First, we observe that the loops remain Gaussian, despite they are now detached from the backbone [Supplemental Material Fig. S5A [44]], and their sizes are unchanged. Second, for the same loop fraction the system with cut loops and the original one with attached loops produce indistinguishable, within the error bar, $R(s)$ of the main chain [Supplemental Material Figs. S5B and S5C [44]]. We conclude that loop attachment and interactions between them do not deform the main chain.

While occupying some volume, loops do not crumple the main chain either. In fact, when we confine the single backbone chain to the same volume density, but without any loops, it becomes more crumpled, yielding a smaller N_e. Indeed, the effective substitution of the unentangled loops by the crumpled backbone in a unit volume results in stronger crumpling and the decrease of the entanglement length [Fig. 4(e) and Supplemental Material Fig. S6 [44]]. The observed value of N_e corresponds to the loop-free system $N_e \approx 70$ kb. These results demonstrate that the loops indeed induce topological screening and decompaction of the main chain; however, their attachment to the backbone plays no role in this effect.

Simulations confirm both the increase in N_e and the mechanism of dilution of entanglements put forward by our theory. The main factor driving this effect is shortening of the main chain, accompanied by screening of entanglements by the unentangled loops Eq. (8).

In good agreement with the theoretical argument Eq. (9) and polymer simulations, we further find that the shapes of $P(s)$ log-derivatives demonstrate a pronounced amplitude irrespective of the loop fraction [Fig. 4(d)]. As we explain above, this amplitude is a signature of increasing N_e of the backbone. In Fig. 4(d), we compare the log-derivatives of $P(s)$ for the simulations of crumpled chains folded into loops with the theoretical curves computed for the original $N_e = 70$ kb (no increase of N_e induced by the loops) corresponding to the loopless case (dashed black curves). It is clear that the model with fixed entanglement length cannot explain the pronounced dip at all loop fractions. On the contrary, as the theory suggests, the increase of λ/g leads to gradual vanishing of the dip [Fig. 2(b) and Supplemental Material Fig. S1 [44]], as long as N_e is fixed.

When we calibrate N_e according to the value of λ/g [Fig. 4(b)] and compute the corresponding theoretical $P(s)$ log-derivatives, we see the restoration of the dip and much better quantitative agreement with simulations [solid black curve in Fig. 4(d)]. Still the agreement is not perfect, since the theory is Gaussian, while crumpled polymers are clearly not [34], which is responsible for subtle deviations between the theory and simulations. Despite this, we conclude that the theory with calibrated entanglement length $N_e = N_e(\lambda/g)$ quantitatively accounts for the behavior of crumpled chains with loops in simulations and restores the dip on the log-derivatives. We thus emphasize that the observed effect of dilution of entanglements in crumpled chains leaves distinct signatures in the $P(s)$ curves—pronounced peak and dip, and leveling at approximately -1 slope—which is evident in the Hi-C data for a broad range of cells and conditions.

III. DISCUSSION

A polymer folded into loops is a new and exciting physical system. Surprisingly, loops affect not only local folding of the polymer, but also long-range organization of the chain, and its topological characteristics. As we show, the interplay between the loop-induced compaction at small scales and arrangement of an array of loops at large scales results in a characteristic shape of the $P(s)$ seen across cell types and organisms. We find that the entanglement length N_e in crumpled chains and the comblike organization of a loopy chain lead to an interesting effect where the loops and the main chain at the scale of a few loops are not crumpled. Moreover, folding into loops further reduces the density of topological entanglements, a phenomenon we refer to as the dilution of entanglements. All these effects together lead to the shape of the $P(s)$ log-derivative curve, similar to the experimental one: with a pronounced peak and dip. Ultimately, this agreement with experiments suggests that chromosomes are folded into loops that are not crumpled (unentangled), and neither is the main chain at the scale of a few loops (approximately 1–2 Mb). Yet, at larger scales (greater than ten loops), the main chain starts forming a crumpled object. This result is a striking diversion from the current understanding of chromosome organization.

Importantly, as we further show in simulations [Supplemental Material Figs. S7A and S7B [44]], compartmentalization of chromosomes does not affect the characteristic contact probability curve of a polymer folded into loops. Indeed, the typical scale of compartmental domains (in humans) is several megabases, which is an order of magnitude larger than the loop size, λ. When block-copolymer interactions derived from experimental Hi-C maps (see Appendix C) are added into simulations with the fixed loops, the resulting $P(s)$ curves do not change significantly (Supplemental Material Fig. S7B [44]]; the constant slope of approximately -1.1 of the loop-free crumpled chain is also unperturbed by the addition of compartments [Supplemental Material Fig. S7A [44]]. This agrees with the observation for the block-copolymer model without loops in Ref. [52]. Our result is also consistent with experiments where depletion of cohesin caused expected changes in the $P(s)$ curves (the loss of the peak and dip on the log-derivative), yet retention and strengthening of compartments [Fig. 2(c)] [31,43].

The dilution of entanglements is a novel exciting phenomenon in crumpled chains folded into loops. We suggest that formation of loops shortens the main chain and stores the material inside the unentangled loops; if loops are short ($\lambda \approx N_e$), they are neither crumpled nor can crumple the main chain, serving as a "reservoir" of unentangled material. This evidently leads to reduction and dilution of topological obstacles along the main chain, both globally (the total amount of the obstacles) and locally (linear density of the obstacles). The latter results in the increase of entanglement length N_e of the main chain and, therefore, decompaction of chromosomes, which counteracts the effective contour length shortening. We suggest a theory explaining how this dilution effect depends on parameters of the loops, which is supported by the simulations. A similar effective stiffening of chromosomes has been recently suggested experimentally [53].

The developed theory allows us to rationalize the shapes of experimental curves in different cell types and upon the change of conditions. Our model shows how sizes of loops, not directly visible in Hi-C data, can be inferred from the shape of experimental $P(s)$ curves. First, the peak on the log-derivative corresponds to the size of the loops with a factor of order of unity [Figs. 5(a) and 5(b), and Supplemental Material Fig. S8 [44]], marginally dependent on the loop fraction. This observation allows us to estimate the typical sizes of chromosome loops from *in vivo* data, yielding a range of $\lambda = 100$–200 kb for various human cells [Fig. 1(b)]. The diagram of $P(s)$ slopes at the peak, and the dip further allows us to infer the typical values of loop fraction parameter d and loop sizes λ from comparison of experimental data points with our theory [Fig. 5(c)]. However, such an analysis of Hi-C curves should be done with caution: It is known that the coarse capture radius in Hi-C can flatten the $P(s)$ at short scales (raising its

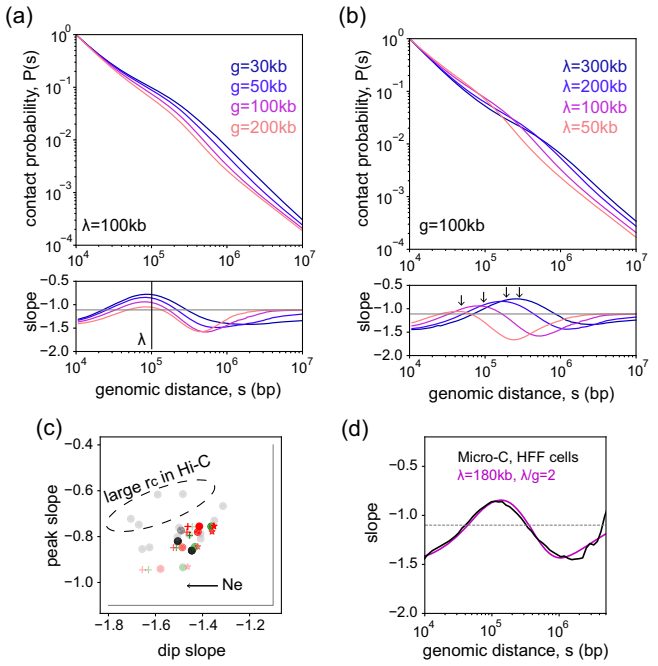

FIG. 5. Behavior of the contact probability curves in the full theory with ideal loops and calibrated $N_e(\lambda/g)$. (a) Change of spacer size g while loop size is fixed, $\lambda = 100$ kb. (b) Change of loop size λ while spacer size is fixed, $g = 100$ kb. Loop fraction increases from red to blue color. (c) Diagram of slopes at the peak and at the dip for various theoretical and experimental curves. Experiment: Hi-C (gray), Micro-C (black). Theory: $\lambda = 100$ (red), $\lambda = 200$ (green); $\varphi = 0.1$ (crosses), $\varphi = 0.2$ (circles), $\varphi = 0.3$ (stars); the dots get less transparent with increase of the loop fraction. (d) Fit of computed experimental Micro-C log-derivative (data from Ref. [38]) by the theory with $\lambda = 180$ kb, $\lambda/g = 2$ and volume density $\varphi = 0.2$. The resulting value of the entanglement length is $N_e \approx 700$ kb; i.e., at the scale of approximately eight loops the main chain is unentangled.

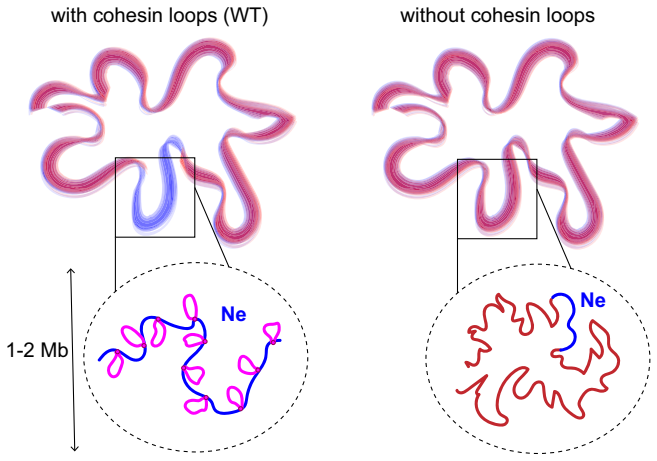

FIG. 6. Chromosomes organization with (left) and without (right) cohesin loops. At large scales $s > N_e$ the chains are crumpled, and at smaller scales $s < N_e$ they remain ideal. Dilution of entanglements due to loops leads to an increase of N_e to $N_e \approx 700$ kb compared to the loop-free case when N_e equals to $N_e \approx 50$–70 kb.

log-derivative) [38,39] [see also Fig. 1(b)]. Accordingly, we see in Fig. 5(c) that a few Hi-C data points have larger amplitudes of the peak slope than the theory can explain. At the same time, we find a rather good agreement of our theory with the Micro-C experiment, where the capture radius is lower, approaching the size of a single nucleosome. The fit presented in Fig. 5(d) suggests that the loop size is $\lambda \approx 180$ kb, which also corresponds to the value derived from the peak position, and $\lambda/g = 2$. Remarkably, an ability to describe experimental data with peak and dip at such large values of loop fraction is due to the presence of the fundamental crossover scale N_e in the crumpled chain: No pure fractal chain with $2 \le d_f \le 3$ yields the dip on the log-derivative for $d \ge 2$ (Supplemental Material Fig. S1 [44]).

These estimates draw a picture of chromosome organization very different from a commonly accepted view (Fig. 6). For the estimated λ and λ/g, the entanglement length (of the main chain) becomes significantly large, $N_e \approx 700$ kb, further suggesting that at a scale of $N_e/g \approx 8$ loops or $s \approx 2$ Mb of genomic distance, a chromosome is virtually unentangled. Indeed, for $\lambda/g \gtrsim 2$ at $s < 1$–2 Mb a chromosome backbone follows the statistics of an ideal chain [both gyration radius $R_g(s_{bb})$ and contact probability $P(s_{bb})$ of the backbone segments are close to approximately s_{bb} and $s_{bb}^{-3/2}$, respectively; see Figs. S4C and S4D in the Supplemental Material [44]], while at larger scales it becomes crumpled. This result is a clear manifestation of the dilution of entanglements due to folding into loops. When the loops are removed, however, N_e drops to approximately 50–70 kb [1], and the chain becomes crumpled in a large range of scales, experimentally 50 kb $< s <$ 5000 kb [30,31] [Fig. 2(c)].

Our theory has several implications and makes testable predictions. Unentangled organization of chromosomes at submegabase scales may be consistent with chromosome dynamics that appear to have Rouse scaling of the mean-squared displacement of individual loci, $\mathrm{MSD}(t) \sim t^{1/2}$ [54] (see Supplemental Material Figs. S7C and S7D [44] and discussion in Appendix C). Our theory also suggests that tracing of the backbone (between the loops) in microscopy, if possible, would produce ideal statistics of the intrachain distances $R(s) \sim s^{1/2}$ up to several Mb with loops (Supplemental Material Fig. S4 [44]), while approximately $s^{1/3}$ without loops (as seen in Ref. [55]). More sparse entanglements in chromosomes with loops can also potentially render different mechanical properties of cell nuclei as compared to the case without loops. In polymer physics, we expect to observe a similar phenomenon of dilution of entanglements in equilibrium melt of linear chains folded into loops, where it can affect dynamics and response to mechanical stress.

While being analytically tractable and powerful in explaining experimental data, our theory has several limitations, that we outline below.

First, our analytical model is limited to independent and exponentially distributed loops and gaps. This allows us to map the sequence of loops and gaps onto the two-state Markov process and obtain a precise expression for the weights of the diagrams. In the dynamic model of loop extrusion there exist nested loops, correlations between the consecutive loop and gap sizes and stalling interactions (collisions) between the neighboring motors, as well as with other proteins on chromosomes. It was shown before [20] that abundant collisions can result in a distribution of the loop sizes which can be approximated by the normal. However, the real distribution of loops and gaps as produced out of dynamic extrusion (without bypassing) is not understood. Our simulations of loopy chains with nonexponential loops (or gaps) size distributions show that while the overall shape of the $P(s)$ curve with loops is preserved, the positions and amplitudes of peak and dip depend on the widths of the distributions (Supplemental Material Fig. S7E [44]). We observe that a narrow distribution of loop sizes with coefficient of variation $c_v < 1$ shifts the peak to the left from the mean loop size λ, while in a wide distribution with $c_v > 1$ shifts the peak to the right (Supplemental Material Fig. S7E, left [44]). A similar effect of the distribution width is observed for the nonexponential gaps, though much more moderate (Supplemental Material Fig. S7E, right [44]). We also note that the wide distribution of loops can result in unrealistically flat peaks. Interestingly, in both cases of narrow $c_v < 1$ and broad $c_v > 1$ distributions, the relative distance between the peak and the dip (in s) is smaller than for the exponential distribution. In the experimental data, the ratio of genomic positions of dip and peak is approximately 10–20 [Fig. 1(b)] and corresponds to the ratio in the model with the exponential distribution of loop sizes.

Second, we consider only equilibrium loops, whereas loops actively extruded by motor proteins turn a polymer into an active or nonequilibrium system. The fixed loops approach relies on the assumption that the time to actively extrude the loop is larger than the time of its passive relaxation. Thus, there exists a critical length scale s^*, such that for loops $\lambda < s^*$ the relaxation is faster than extrusion, and our assumption largely holds. Quantitative estimates (see Appendix D) indicate that for the upper limit of the extrusion speed of $r = 1$ kb/s [56], the Kuhn segment $l_k = 4$ kb and Rouse diffusion coefficient $D_R = 10^{-2}$ μm^2 s$^{-1/2}$ [54] the critical equilibrium scale can be as large as $s^* = 100 \div 1000$ kb $\gtrsim \lambda$. Another experimental estimate from Ref. [54] is that a chain of approximately 500 kb equilibrates in approximately 40 min; extrapolating to 100 kb loops, it gives approximately 2 min to equilibrate. Loops of $\lambda \approx 100$ kb can be extruded in as little as approximately 2 min if the speed is 1 kb/sec or in approximately 10 min if experimentally measured cohesin residence time is used. Thus, at the lower limit of this range, loops may not be fully equilibrated. We note that equilibration of the loops, and restoration or extinction dynamics of topological obstacles in the steady state would create a nontrivial interplay, whose consequences on the contact probability are yet to be understood.

Third, for the sake of analytical tractability, we employ here a Gaussian model mapping a fractal chain onto the fractional Brownian motion [2]. We explicitly rely on the Gaussianity of the chain by making use of the mean-field connection between the equilibrium spatial distance and the contact probability Eq. (1). Accordingly, the spatial distances in loops are computed by treating them as fractional Brownian motion (fBm) bridges, which allow us to exploit the effective Hamiltonian of fractal polymer states [2,35]. However, it is well known that crumpled chains are characterized by a non-Gaussian probability density of the end-to-end distance, as suggested by the general Redner–des Cloizeaux distribution and confirmed in recent simulations [34]. As a result, the $P(s)$ exponent of a loopless crumpled chain approximately equal to -1.1 is somewhat smaller than the mean-field prediction $-3/d_f = -1$. Furthermore, it has been shown in Refs. [17,18] and is also seen here in Figs. 7(a) and 7(b) that the crossover from ideal to crumpled behavior in $R^2(s)$ and $P(s)$ [while being sensitive to the value of the cutoff radius used in computation of $P(s)$] occurs at not precisely the same length scales s. Still, these differences are restricted to short distances $s < N_e$, while at large scales the contact probability of the chain can be approximated by the effective ("Gaussian") fractal dimension $d_f \approx 3/1.1 \approx 2.7$ reproducing the asymptotic $P(s)$ exponent of crumpled rings.

Fourth, we do not consider very dense arrays of loops, bottle brushes, that fold chromosomes into elongated compacted bodies (during mitosis [57], meiosis [58], and in WaplKO). At $\lambda/g > 4$, the spatial size of a Gaussian loop reaches the spatial size of the Gaussian gap, marking a transition to the bottle-brush regime, when rigidity of the chain can become dominant. As shown in Ref. [59] for comblike chains with linear side groups, in this regime (specifically, a loosely grafted bottle brush) the gaps

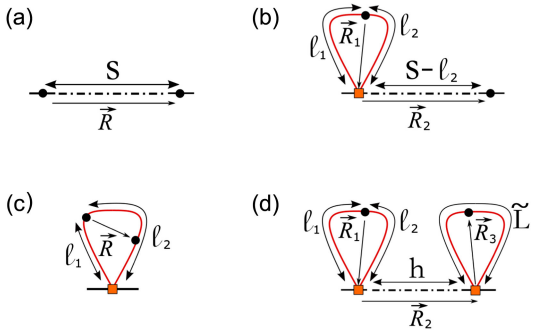

FIG. 7. Four diagrams contributing to the contact probability between two sites (depicted as black dots) of polymer chain with a quenched disorder of random loops (depicted in red). The loop extrusion factors are depicted as orange squares.

become fully stretched due to osmotic pressure generated by the side chains. In case of a crumpled backbone, a nontrivial interplay between the stretching and decompaction (increase of N_e) can happen in the dense regime. Consistently, the bottle-brush stiffening might be responsible for a slight deepening of the dip observed in Wapl knockout experiments [Fig. 2(c)], where chromosomes acquire a visibly different, noodlelike, morphology (known as vermicelli chromosomes) [40]. Since Wapl protein is responsible for cohesin unloading, Wapl depletion has two effects: an increase in the cohesin residence time, which results in larger loops, and an approximately twofold increase in the amount of cohesin on chromosomes, thus reducing g; together, this turns a chromosome into a dense bottle brush of loops, where our the theory does not apply.

In summary, we develop an analytical theory of a crumpled polymer folded into loops and reveal a novel topological phenomenon in such a system. We demonstrate that information about loops is contained in the shape of experimentally measurable contact probability curve $P(s)$ and primarily in its log-derivative. Our theory quantitatively reproduces the experimental curves and allows us to infer parameters of the loops *in vivo*. Furthermore, we propose that the density of entanglements in chromosomes is reduced due to folding into loops, resulting in chromosomes that are not crumpled at scales up to approximately 1–2 Mb. Together, our findings demonstrate that folding of a polymer into loops not only changes its conformational characteristics across scales, but also reduces the topological constraints in the polymer system.

ACKNOWLEDGMENTS

We thank Mehran Kardar, Alexander Grosberg, Michael Rubinstein, Ralf Everaers, and Mikhail Tamm for valuable discussions on the subject of the paper. L. M. acknowledges support from the NIH Common Fund 4D Nucleome Program, Grant No. HG011536, Center for 3D Structure and Physics of the Genome, and NHGMS NIH Grant R01GM114190. The work of K. P. and B. S. is supported by the Russian Science Foundation (Grant No. 21-73-00176). K. P. also acknowledges the support of the Programme d'investissements d'avenir (LabEx DEEP) at Institut Curie, Paris, France. The work of S. B. on the ideal chain model has been supported by the Russian Science Foundation (Grant No. 20-72-00170). S. B. also acknowledges support from James S. McDonnell Foundation in 2017–2020.

APPENDIX A: DERIVATION OF THE CONTACT PROBABILITY FOR A FRACTAL POLYMER CHAIN WITH LOOPS

1. Basic properties of equilibrium ideal Gaussian chains

In the absence of cohesin-mediated loops, the probability distribution of the separation vector $\vec{R}$ between two sites of an equilibrium ideal linear Gaussian chain separated by contour distance s is given by (see Refs. [12,32,33])

$$P_{\text{free}}(\vec{R}|s) = \left(\frac{3}{2\pi\sigma^2_{\text{free}}[s]}\right)^{3/2} \exp\left(-\frac{3R^2}{2\sigma^2_{\text{free}}[s]}\right), \quad \text{(A1)}$$

where

$$\sigma^2_{\text{free}}[s] = l_p b^2 s, \quad \text{(A2)}$$

and b^2 is the mean square length of a chain segment, and l_p is the persistence length. The Gaussian distribution of the separation vector (A1) is valid for $s \gg l_p$.

For an equilibrium ideal Gaussian bridge having size L, the probability distribution of the separation vector $\vec{R}$ between two sites separated by contour distance s ($<L$) is given by

$$P_{\text{bridge}}(\vec{R}|s,L) = \left(\frac{3}{2\pi\sigma^2_{\text{bridge}}[s,L]}\right)^{3/2} \times \exp\left(-\frac{3R^2}{2\sigma^2_{\text{bridge}}[s,L]}\right), \quad \text{(A3)}$$

where (see Ref. [12])

$$\sigma^2_{\text{bridge}}[s,L] = \frac{l_p b^2 s(L-s)}{L}. \quad \text{(A4)}$$

2. Subdiffusive fBm trajectories and the effective Hamiltonian

To take into account non-Markovian properties of the trajectory at values of fractal dimension $d_f > 2$, we consider the class of fBm with the Hurst parameter $H = 1/d_f$ as a model to the fractal polymer fiber. To begin with, define the trajectory of a discrete random walk, or, similarly, a conformation of a polymer chain in the three-dimensional space by a set of coordinates $\{\boldsymbol{X}\} = \{\boldsymbol{x}_0, \boldsymbol{x}_1, \ldots, \boldsymbol{x}_N\}$. There exists a unique stationary measure $P(\boldsymbol{X})$ over the realizations of the walk $\boldsymbol{X}$, which satisfies

$$\begin{aligned} p((\boldsymbol{x}_k - \boldsymbol{x}_m) = \boldsymbol{y}) &= \int d\boldsymbol{X} P(\boldsymbol{X}) \delta(\boldsymbol{x}_k - \boldsymbol{x}_m - \boldsymbol{y}) \\ &= \left(\frac{3}{2\pi l_p b^2 s^{2/d_f}}\right)^{3/2} \exp\left(-\frac{3\boldsymbol{y}^2}{2 l_p b^2 s^{2/d_f}}\right); \\ s &= |k-m| \end{aligned} \quad \text{(A5)}$$

for all k, m, and some fixed constant d_f called fractal dimension of the walk.

It the recent works of one of us [2,4,35], it has been shown that in the limit of large N for the subdiffusive

($d_f > 2$) fBm, one can write down $P(\boldsymbol{X})$ as a Gibbs measure with a pairwise quadratic Hamiltonian:

$$P(\boldsymbol{X}) = \frac{1}{Z}\exp[-V(\boldsymbol{X})], \qquad Z = \int \exp[-V(\boldsymbol{X})]d\boldsymbol{X},$$
$$V(\boldsymbol{X}) = \sum_{i<j} A_{ij}(\mathbf{x}_i - \mathbf{x}_j)^2, \tag{A6}$$

with a proper choice of interactions coefficients A_{ij} (here Z is the partition function, and we use lowercase and uppercase bold letters to denote vectors in three-dimensional and $(3 \times N)$-dimensional space, respectively). In particular, if the coefficients A_{km} depend only on the chemical distance between monomers $|k - m| = s$, so that $A_{km} = A(s)$, and if for $s \gg 1$ $A(s)$ decays algebraically

$$A(s) \sim cs^{-\gamma} \tag{A7}$$

with some $c > 0$, then depending on γ there are three possible asymptotic regimes of the chain statistics:

(1) If $\gamma \leq 2$, all monomers (points of the trajectory) asymptotically merge, and

$$\langle(\mathbf{x}_k - \mathbf{x}_m)^2\rangle \to 0 \quad \text{when } N \to \infty \tag{A8}$$

regardless $s = |k - m|$.

(2) If $\gamma > 3$, the interaction is irrelevant, and the large-scale properties of the trajectory are indistinguishable from the standard Brownian motion with $d_f = 2$.

(3) Finally, and most interesting, if $2 < \gamma < 3$ the relation Eq. (A5) holds for $1 \ll s \ll N$ with some renormalized $\bar{b}(c, \gamma)$ and a nontrivial fractal dimension

$$d_f = \frac{2}{\gamma - 2}. \tag{A9}$$

The value of $\gamma = 3$ is critical, giving rise to the logarithmic corrections to Eq. (A5). Note that the conventional beads-on-a-string model corresponds to the choice

$$A(s) = \frac{3}{2b^2}\delta_{s,1}. \tag{A10}$$

Now we can generalize Eq. (A2) to an arbitrary fractal dimension $d_f \geq 2$:

$$\sigma^2_{\text{free}}[s] = l_p b^2 s^{2/d_f}. \tag{A11}$$

Using the effective Hamiltonian (A6), we generalize Eq. (A4) for a fractal bridge in the next section.

3. fBm bridge

To get the distribution between sites inside a bridge having length L (measured in numbers of edges between monomeric units), let us notice that a fBm chain becomes a fBm bridge if and only if the separation vector between the first and last site is $\mathbf{0}$ (i.e., $\mathbf{x}_0 = \mathbf{x}_L$). By definition of conditional probability, we have for any s the following probability distribution function:

$$P_{\text{bridge}}(\mathbf{r}|s, L) = \frac{\mathbb{P}_{\text{free}}[\mathbf{x}_s - \mathbf{x}_0 = \mathbf{r} \cap \mathbf{x}_L - \mathbf{x}_0 = \mathbf{0}]}{\mathbb{P}_{\text{free}}[\mathbf{x}_L - \mathbf{x}_0 = \mathbf{0}]}, \tag{A12}$$

where $\mathbb{P}_{\text{free}}[\cdot]$ is the probability measure Eq. (A6) in a free polymer chain. If chain sections $0, \ldots, s$ and $s, \ldots, L$ were independent, one could represent the numerator as product of two probabilities $P_{\text{free}}(\mathbf{r}|s)$ and $P_{\text{free}}(\mathbf{r}|L - s)$ and arrive at Eq. (A4) valid for $d_f \neq 2$. But a general fBm walk for $d_f \neq 2$ has long-range memory; therefore, we need a more delicate technique to express the probability above.

Using the Gibbs distribution Eq. (A6), we can write

$$P_{\text{bridge}}(\mathbf{r}|s, L) = \frac{\int \delta(\mathbf{x}_s - \mathbf{x}_0 - \mathbf{r})\delta(\mathbf{x}_L - \mathbf{x}_0) \cdot P(\mathbf{X})D\mathbf{X}}{\int \delta(\mathbf{x}_L - \mathbf{x}_0) \cdot P(\mathbf{X})D\mathbf{X}}. \tag{A13}$$

The denominator is calculated straightforwardly from Eq. (A5), and proceeding with the nominator we can Fourier transform the delta functions

$$P_{\text{bridge}}(\mathbf{r}|s, L) = \left(\frac{2\pi\sigma^2_{\text{free}}[L]}{3}\right)^{3/2} \cdot \cdot \frac{1}{(2\pi)^6}\int G(\mathbf{q}, \mathbf{q}', \mathbf{r}, s, L)d\mathbf{q}d\mathbf{q}', \tag{A14}$$

where the Green's function has the following form [putting all formulas in Eq. (A6) together]:

$$\begin{aligned} G(\mathbf{q}, \mathbf{q}', \mathbf{r}, s, L) &= \frac{1}{Z}\int d\mathbf{x}_0, \ldots, d\mathbf{x}_L \exp\Bigg(-\frac{1}{2}\sum_{i,j} A_{ij}(\mathbf{x}_j - \mathbf{x}_i)^2 \\ &\quad + i\mathbf{q}(\mathbf{x}_s - \mathbf{x}_0 - \mathbf{r}) + i\mathbf{q}'(\mathbf{x}_L - \mathbf{x}_0)\Bigg) \\ &= \frac{1}{Z}\int d\mathbf{x}_0, \ldots, d\mathbf{x}_L \exp\Bigg(-\frac{1}{2}\sum_{i,j} a_{ij}\mathbf{x}_i\mathbf{x}_j \\ &\quad + i\mathbf{q}(\mathbf{x}_s - \mathbf{x}_0) + i\mathbf{q}'(\mathbf{x}_L - \mathbf{x}_0) - i\mathbf{q}\mathbf{r}\Bigg) \\ &= \frac{1}{Z}\exp(-i\mathbf{q}\mathbf{r})\int d\mathbf{x}_0, \ldots, d\mathbf{x}_L \exp\left(-\frac{1}{2}\mathbf{X}^T\mathbb{A}\mathbf{X} + \mathbf{B}^T\mathbf{X}\right), \end{aligned} \tag{A15}$$

where the new matrix $\mathbb{A} = \|a_{ij}\|$ is introduced

$$a_{ij} = \begin{cases} 2\sum_k A_{ik}, & i = j, \\ -2A_{ij}, & i \neq j, \end{cases} \tag{A16}$$

and the new vector $\mathbf{B} \in \mathbb{R}^{3(L+1)}$ consists of $L+1$ parts

$$\mathbf{b}_\alpha = i\mathbf{q}(\delta_{s\alpha} - \delta_{0\alpha}) + i\mathbf{q}'(\delta_{L\alpha} - \delta_{0\alpha}), \qquad \alpha \in \{0, \ldots, L\}. \tag{A17}$$

Using new notations, we can express the full partition function Z [again from Eq. (A6)]

$$Z = \int d\mathbf{x}_0, \ldots, d\mathbf{x}_L \exp\left(-\frac{1}{2}\mathbf{X}^T \mathbb{A} \mathbf{X}\right) = \sqrt{\frac{1}{\det(\mathbb{A}/2\pi)}}. \tag{A18}$$

Using the resulting Gaussian-like integral in Eq. (A15), we get a new form of the Green's function:

$$G(\mathbf{q}, \mathbf{q}', \mathbf{r}, s, L) = \exp(-i\mathbf{q}\mathbf{r}) \exp\left(\frac{1}{2}\mathbf{B}^T \mathbb{A}^{-1} \mathbf{B}\right). \tag{A19}$$

Let us denote ω_p and $\mathbf{A}_p$ $(p = 0, 1, \ldots, L)$—eigenvalues and eigenvectors of $\mathbb{A}$, respectively, ordered from the smallest eigenvalue to the largest. Using scalar (inner) products

$$\boldsymbol{\beta}_p = \langle \mathbf{B}, \mathbf{A}_p \rangle = i\mathbf{q}(a_p^s - a_p^0) + i\mathbf{q}'(a_p^L - a_p^0), \tag{A20}$$

where a_p^s—the (s)th component of the vector $\mathbf{A}_p$—we can express

$$\log G(\mathbf{q}, \mathbf{q}', \mathbf{r}, s, L) = -i\mathbf{q}\mathbf{r} + \frac{1}{2}\sum_{p=0}^{L} \omega_p^{-1} |\boldsymbol{\beta}_p|^2. \tag{A21}$$

Substituting Eq. (A21) into Eq. (A14) gives us

$$\begin{aligned} P_{\text{bridge}}(\mathbf{r}|s, L) &= \frac{(2\pi\sigma^2_{\text{free}}[L])^{3/2}}{3^{3/2}(2\pi)^6} \int d\mathbf{q} \int d\mathbf{q}' \\ &\times \exp\left(-i\mathbf{q}\mathbf{r} + \frac{1}{2}\sum_{p=0}^{L} \omega_p^{-1} |\boldsymbol{\beta}_p|^2\right) = \ldots \int d\mathbf{q} \int d\mathbf{q}' \\ &\times \exp\Bigg(-i\mathbf{q}\mathbf{r} + \frac{1}{2}\sum_{p=0}^{L} \omega_p^{-1} |i\mathbf{q}(a_p^s - a_p^0) \\ &+ i\mathbf{q}'(a_p^L - a_p^0)|^2\Bigg) = \ldots \int d\mathbf{q} \int d\mathbf{q}' \\ &\times \exp\left(-i\mathbf{q}\mathbf{r} - \frac{1}{2}\sum_{p=0}^{L} \omega_p^{-1} |\mathbf{q}(a_p^s - a_p^0) + \mathbf{q}'(a_p^L - a_p^0)|^2\right). \end{aligned} \tag{A22}$$

This is a double Gaussian integral, which can be calculated explicitly through parentheses expansion and grouping components of $\mathbf{q}$ and $\mathbf{q}'$ into pairs:

$$P_{\text{bridge}}(\mathbf{r}|s, L) = \left(\frac{1}{2\pi}\frac{3}{\frac{9\det\Sigma}{l_p b^2 L^{2H}}}\right)^{3/2} \exp\left(-\frac{3\mathbf{r}^2}{2}\frac{1}{\frac{3\det\Sigma}{\sigma_{22}}}\right), \tag{A23}$$

where elements of the matrix Σ are

$$\begin{aligned} \sigma_{11} &= \sum_{p=0}^{L} \omega_p^{-1} |a_p^s - a_p^0|^2, \\ \sigma_{22} &= \sum_{p=0}^{L} \omega_p^{-1} |a_p^L - a_p^0|^2, \\ \sigma_{12} &= \sigma_{21} = \sum_{p=0}^{L} \omega_p^{-1} (a_p^s - a_p^0)(a_p^L - a_p^0). \end{aligned} \tag{A24}$$

Importantly, the elements of matrix Σ have the meaning of the mean-square distances between corresponding monomers. Indeed, expressing these distances as sums over normal coordinates $\mathbf{u}_p = \langle \mathbf{X}, \mathbf{A}_p \rangle$ and using the equipartition theorem, which determines the average amplitudes of the normal modes at equilibrium (see Ref. [2] for more details), one gets $\langle \mathbf{u}_\alpha, \mathbf{u}_\beta \rangle = 3\omega_\alpha^{-1}\delta_{\alpha\beta}$ and, therefore,

$$\begin{aligned} \langle (\mathbf{x}_s - \mathbf{x}_0) \rangle^2 &= 3\sigma_{11}, \\ \langle (\mathbf{x}_L - \mathbf{x}_0) \rangle^2 &= 3\sigma_{22}, \\ \langle (\mathbf{x}_s - \mathbf{x}_0)(\mathbf{x}_L - \mathbf{x}_0) \rangle &= 3\sigma_{12}. \end{aligned} \tag{A25}$$

The left-hand sides can be easily derived from properties of the fBm:

$$\begin{aligned} \sigma_{11} &= l_p b^2 s^{2H}/3 = \sigma^2_{\text{free}}[s]/3, \\ \sigma_{22} &= l_p b^2 L^{2H}/3 = \sigma^2_{\text{free}}[L]/3, \\ \sigma_{12} &= \frac{l_p b^2}{6}(L^{2H} + s^{2H} - (L-s)^{2H}) \\ &= \frac{1}{6}(\sigma^2_{\text{free}}[L] + \sigma^2_{\text{free}}[s] - \sigma^2_{\text{free}}[L-s]). \end{aligned} \tag{A26}$$

Getting back to Eq. (A23), we obtain

$$\begin{aligned} &\sigma^2_{\text{bridge}}[s, L] \\ &= \frac{3\det\Sigma}{\sigma_{22}} = 3\sigma_{11}\left(1 - \frac{\sigma_{12}^2}{\sigma_{11}\sigma_{22}}\right) \\ &= \sigma^2_{\text{free}}[s]\left(1 - \frac{(\sigma^2_{\text{free}}[L] + \sigma^2_{\text{free}}[s] - \sigma^2_{\text{free}}[L-s])^2}{4\sigma^2_{\text{free}}[s]\sigma^2_{\text{free}}[L]}\right). \end{aligned} \tag{A27}$$

Notice that when $H = 1/2$ (standard Brownian motion),

$$\sigma^2_{\text{bridge}}[s,L] = \sigma^2_{\text{free}}[s]\frac{L-s}{L} = \frac{l_p b^2 s(L-s)}{L}, \quad \text{(A28)}$$

which naturally matches Eq. (A4).

4. Conditional contact probabilities for different diagrams

For an arbitrary polymer chain, the pairwise contact probability between two sites separated by linear distance s is given by

$$P(s) = \text{Prob}[R(s) < a_0] \approx \frac{4}{3}\pi a_0^3 \int P(\vec{R}|s)\delta(\vec{R})d^3R = \frac{4}{3}\pi a_0^3 P(0|s), \quad \text{(A29)}$$

where a_0 is a cutoff contact radius, and $P(\vec{R}|s)$ is the probability distribution of the intersites separation vector $\vec{R}$. In derivation of Eq. (A29), we assume that $a_0 \ll \sqrt{\langle R^2\rangle}$.

From Eq. (A29), we immediately find that the contact probability between two sites of a fBm chain with fractal dimension d_f and free ends behaves as $1/s^{3/d_f}$, where s is the contour separation between the points.

How does this result change in the presence of random loops? For a given realization of the random loops array, one should consider four scenarios of the relative positions of the two sites as schematically shown in Fig. 7. Here we neglect the diagrams corresponding to the nested and overlapping loops configurations as they rarely occur under the conditions of the interphase. Under the assumption of equilibrium loops (quenched disorder of loops), the resulting contact probability is given by the sum

$$P(s) = \frac{4}{3}\pi a_0^3 \sum_{i=a,b,c,d} \langle p_{(i)}(s|\{A\}_i)\rangle, \quad \text{(A30)}$$

where

$$p_{(i)}(s|\{A\}_i) = (2\pi\sigma^2_{(i)}[s|\{A\}_i])^{-3/2} \quad \text{(A31)}$$

is the contact probability conditional to the particular class of subchain. In what follows, we work out exact expressions for $\sigma^2_{(i)}[s|\{A\}_i]$.

First, let us consider Fig. 7(a). In the presence of an arbitrary number of loops between the two points of interest the variance of their physical separation reads

$$\sigma^2_{(a)}[s|x] = \sigma^2_{\text{free}}[(1-x)s], \quad \text{(A32)}$$

where x $(0 \le x < 1)$ denotes the fraction of the subchain length occupied by the loops. In other words, the intervening loops lead to the effective reduction of the contour distance between the points.

Next, let us consider a subchain of linear size s with one end belonging to the gap region and another end belonging to the loop. The loop containing one of two sites of interest can be paramterized by the lengths l_1 and l_2, as shown in Fig. 7(b). Clearly, the separation vector $\vec{R}$ between two sites can be represented as a sum of mutually independent zero mean Gaussian random vectors, $\vec{R}_1$ and $\vec{R}_2$, whose statistical properties are described, respectively, by the normal distributions (A1) and (A3) under an appropriate choice of parameters. Recalling that the sum of independent Gaussian variables has normal statistics with the variance given by the sum of variances of the underlying terms, we obtain

$$\sigma^2_{(b)}[s|l_1,l_2,x] = \sigma^2_{\text{bridge}}[l_2, l_1+l_2] + \sigma^2_{\text{free}}[(1-x)(s-l_2)], \quad \text{(A33)}$$

where $0 \le x < 1$, $l_1 \ge 0$, and $0 \le l_2 \le s$. Now, x is the fraction of contour length occupied by loops in the segment of size $s - l_2$ enclosed between the loop base and the remaining end of the subchain.

Now let us consider a subchain located inside a loop; see Fig. 7(c). Then,

$$\sigma^2_{(c)}[s|l_1,l_2] = \sigma^2_{\text{bridge}}[s, l_1+l_2], \quad \text{(A34)}$$

where $l_1 \ge 0$ and $l_2 \ge s$.

Finally, for the last diagram, Fig. 7(d),

$$\sigma^2_{(d)}[s|l_1,l_2,h,\tilde{l}_1,\tilde{l}_2] = \sigma^2_{\text{bridge}}[l_2, l_1+l_2] + \sigma^2_{\text{free}}[(1-x)h] + \sigma^2_{\text{bridge}}[\tilde{l}_2, \tilde{l}_1+\tilde{l}_2], \quad \text{(A35)}$$

where $\tilde{l}_1 = \tilde{L} + h + l_2 - s$, $\tilde{l}_2 = s - h - l_2$, $l_1 \ge 0$, $0 \le l_2 \le s$, $0 \le h \le s - l_2$, $0 \le x \le 1$, and $\tilde{L} \ge s - l_2 - h$. Here, x is the fraction of contour length occupied by loops in the segment of size $s - l_2 - \tilde{l}_2$ enclosed between two loops depicted in Fig. 7(d).

5. Statistical weights of the diagrams

To perform the averaging procedure over disorder of loops assumed in Eq. (A30), one needs to know the probability distributions of the random variables $\{A\}_i$, which parametrize the contributions coming from different types of the diagrams [Figs. 7(a)–7(d)].

Let us treat the sizes of the loops and of the gaps as the independent random variables having exponential probability distributions with $\alpha_l = \lambda^{-1}$ and $\alpha_g = g^{-1}$. Then, in order to derive the statistical weights of the diagrams, it is convenient to introduce an auxiliary Markov jump process with two states "Loop" and "Gap" in continuous time where time intervals are measured in the units of the polymer contour length. Clearly, the statistics of the random pattern of alternating loops and gaps is analogous

to the joint statistics of the time intervals which the Markov process spends in the Loop (L) and the Gap (G) states in the course of its stochastic dynamics.

Based on this analogy, we can express the statistical weight of Fig. 7(a) as follows:

$$\mathcal{W}_a(x|s) = p_g g(G,s|G,0)\mathcal{F}(x|s), \tag{A36}$$

where $p_g = (\alpha_l/\alpha_g + \alpha_l)$ is the probability to find the statistically stationary Markov process in the state Gap if one visits it in a random time moment (i.e., the probability that a randomly chosen point of the polymer belongs to a gap), $g(G,s|G,0) = (1/\alpha_g + \alpha_l)(\alpha_l + \alpha_g e^{-(\alpha_l+\alpha_g)s})$ is the probability to find the Markov jump process in the state Gap after time s under the condition that it starts in the state Gap (i.e., the probability that the second point, which is separated by contour distance s from the first point, also belongs to a gap region), and $\mathcal{F}(x|s)$ is the probability distribution of the random variable x representing the fraction of time that the Markov process spent in the state Loop under the condition that it starts in the state Gap and find itself in the state Gap after the time s (i.e., x is the fraction of the contour length occupied by loops for a segment whose both ends belong to the gap regions), which is given by (see Ref. [41])

$$\begin{aligned}\mathcal{F}(x|s) = \frac{\alpha_g+\alpha_l}{\alpha_l+\alpha_g e^{-(\alpha_l+\alpha_g)s}}\Bigg\{ & e^{-\alpha_g s}\delta(x) \\ & + \left(\frac{\alpha_g\alpha_l(1-x)s^2}{x}\right)^{1/2} I_1\left[2\sqrt{\alpha_g\alpha_l x(1-x)s^2}\right] \\ & \times e^{-\alpha_g(1-x)s-\alpha_l x s}\Bigg\},\end{aligned} \tag{A37}$$

with $I_1[x]$ denoting the modified Bessel function of the first kind [60].

Next, the statistical weight of configurations responding to Fig. 7(b) is

$$\mathcal{W}_b(l_1,l_2,x|s) = 2p_l\rho(l_1)\rho(l_2)g(G,s|G,l_2)\mathcal{F}(x|s-l_2), \tag{A38}$$

where $p_l = (\alpha_g/\alpha_g + \alpha_l)$ denotes the probability to find the statistically stationary Markov process in the state Loop if one visits it in a random time moment, the factors $\rho(l_1) = \alpha_l e^{-\alpha_l l_1}$ and $\rho(l_2) = \alpha_l e^{-\alpha_l l_2}$ represent, respectively, the probability densities of the random time l_1 elapsed since the last entrance to the state Loop and of the random time l_1 remaining before the next jump to the state Gap, and $\mathcal{F}(x|s-l_2)$ is the probability distribution of the fraction of time x that the Markov process spent in the state Gap under the condition that it starts in the state Gap and finds itself also in the state Gap after the time $s-l_2$. Note also that factor 2 in Eq. (A38) arises due to the left-right symmetry in the choice of point which is assumed to reside on the loop.

Similarly, the statistical weight of configurations responding to Fig. 7(c) is

$$\mathcal{W}_c(l_1,l_2|s) = p_l\rho(l_1)\rho(l_2). \tag{A39}$$

Finally, the statistical weight of subchains described by Fig. 7(d) is given by

$$\begin{aligned}\mathcal{W}_d(l_1,l_2,h,x,\tilde{L}|s) = {} & p_l\rho(l_1)\rho(l_2)\rho(\tilde{L})\alpha_g \\ & \times g(G,l_2+h|G,l_2)\mathcal{F}(x|h).\end{aligned} \tag{A40}$$

Substituting Eqs. (A32)–(A35) and (A36)–(A40) in Eq. (A30), we come to the final expressions of contact probability in the fractal polymer model (see Supplemental Material [44]).

6. Entanglement length N_e

Now let us add another ingredient to our model of a fractal chain with loops, the entanglement length N_e. This parameter allows us to describe the crossover in r^2 between two regimes of (s):

$$r^2(s|N_e) = \begin{cases} s l_p b^2 & \text{for } l_p < s \le N_e, \\ s^{2H} N_e^{1-2H} l_p b^2 & \text{for } s \ge N_e, \end{cases} \tag{A41}$$

where $H = 1/d_f$ and d_f is the fractal dimension. For $d_f = 3$, this behavior accounts for the real crumpled polymer chains, such as a ring from the melt of unknotted noncatenated rings [16,34]. Thus, the physical meaning of N_e is the scale of the minimal crumple, below which the crumpled polymer does not feel topological constraints in the system and has ideal statistics.

Expression Eq. (A41) is nonsmooth, making the analysis of log-derivatives of the respecting curves problematic. Thus, it is worthwhile to smooth Eq. (A41) by averaging over a certain distribution of N_e. If we take N_e as an exponentially distributed random variable x with mean N_e, we can average r^2 above and use it as a new function $\sigma^2_{\text{free}}(s,N_e)$:

$$\begin{aligned}&\sigma^2_{\text{free}}(s,N_e) \\ &= \int_0^\infty r^2(s|x)\times\frac{e^{-x/N_e}}{N_e}dx \\ &= \frac{l_p b^2 s^{2H}}{N_e}\int_0^s x^{1-2H}\times e^{-x/N_e}dx + \frac{l_p b^2 s}{N_e}\int_s^\infty e^{-x/N_e}dx \\ &= l_p b^2\left(N_e\left(\frac{s}{N_e}\right)^{2H}\gamma\left(2-2H,\frac{s}{N_e}\right) + s e^{-s/N_e}\right),\end{aligned} \tag{A42}$$

where $\gamma(x,y)$ is the lower incomplete gamma function. Since $l_p \ll N_e$ one can substitute the lower bound by zero

in Eq. (A42). The resulting averaged $\sigma^2_{\text{free}}(s, N_e)$ is substituted instead of Eq. (A11) in Eq. (A27) and Eqs. (A32)–(A35). Noticeably, since all bridges and the backbone are independent, we can use different entanglement lengths, one for bridges and one for the backbone.

APPENDIX B: DERIVATION OF THE EFFECTIVE VOLUME DENSITY OF A CHAIN FOLDED INTO LOOPS

The increase of the entanglement length for a chain with loops is associated with the decrease of the effective volume density of the polymer, according to the formula Eq. (6). The effective Kuhn volume density φ_k^{eff} relevant for the entanglements, of a crumpled polymer with loops can be expressed as follows:

$$\varphi_k^{\text{eff}} = \frac{NMv_k}{l_k(d+1)} \frac{1}{V_0 - V_{\text{loops}}}, \tag{B1}$$

where $v_k \propto l_k^3$ and l_k are the volume and the size of the Kuhn segment, respectively; M is the number of chains strongly overlapping with each other (the overlap parameter [32]) in the volume V_0 of a single chain; $d = \lambda/g$ is the loop fraction parameter; $V_0 = R_0^3$ is the volume occupied by one chain, i.e., the cubed size of its backbone; V_{loops} is the total volume of the loops. The spatial size of the backbone is controlled by its contour length, $N_0 = N/(d+1)$, the entanglement length N_e, and the Kuhn length l_k as follows:

$$R_0 = (N_0/N_e)^{1/3}(N_e/l_k)^{1/2} l_k b, \tag{B2}$$

therefore,

$$V_0 = R_0^3 = \frac{N}{d+1} N_e^{1/2} l_k^{3/2} b^3. \tag{B3}$$

Since each loop is unentangled, their spatial size can be approximated by the size of a Gaussian bridge, $R^2_{\text{loop}} = \lambda l_k b^2/4$, and their overlap with each other can be neglected. The mean number of the loops occupying the volume V_0 reads $n_{\text{loops}} = M(N/d+1)(d/\lambda)$. Then, one can estimate the total volume of the loops as follows:

$$V_{\text{loops}} = n_{\text{loops}} R^3_{\text{loop}} = \frac{1}{8}\lambda^{1/2} d (l_k b^2)^{3/2} \frac{MN}{d+1}. \tag{B4}$$

The total number of chains M populating the volume V_0 is determined by the total Kuhn volume density of the system $\varphi_k^{(0)} = \varphi_k^{\text{eff}}(d=0)$ and the entanglement length N_e as

$$M = \frac{\varphi_k^{(0)} l_k V_0}{N v_k} = \frac{\varphi_k^{(0)} b^3}{v_k(d+1)} N_e^{1/2} l_k^{5/2}. \tag{B5}$$

Collecting Eqs. (B1), (B3), (B4) and (B5) together, one arrives at the following expression for the effective volume density of the backbone:

$$\varphi_k^{\text{eff}} = \frac{\varphi_k^{(0)}}{1 + d(1 - c_\alpha \varphi_k^{(0)} \lambda^{1/2})}, \tag{B6}$$

where the constant c_α depends on the parameters of the fiber, $c_\alpha = l_k^{5/2} b^3/(8v_k) \propto l_k^{-1/2}$. In particular, c_α depends on the numerical coefficients in the expression for the excluded volume of the Kuhn segment $v_k \propto l_k^3$, which are determined by the microscopic structure of the fiber. Fitting the resulting $N_e = N_e(\varphi_k^{\text{eff}})$ as predicted by Eq. (B6) to the one computed in simulations, we find the phenomenological expression for $c_\alpha \approx 0.02 l_k^{-1/2}$.

The structure of Eq. (B6) can be understood as follows. Without loops ($d = 0$), the backbone resembles the original crumpled chain with effective volume density $\varphi_k^{(0)}$. If the loops are sufficiently short so that their volume can be neglected, then the main contribution to the decreased volume density comes from the backbone shortening, which yields the factor $d+1$ in the denominator. In a general case, the loops occupy a certain volume partially compensating the effect of the backbone shortening.

To understand better the role of the compensation effect, it is instructive to introduce the entanglement length $\tilde{N}_e$ of a single ($M = 1$) crumpled chain without loops of the same length N and same Kuhn volume density $\varphi_k^{(0)}$. Clearly from Eq. (B5), $\tilde{N}_e$ is controlled by the volume density of the chain, $\tilde{N}_e \propto (\varphi_k^{(0)})^{-2}$. Then, the combination $c_\alpha \varphi_k^{(0)} = \frac{1}{8}\tilde{N}_e^{-1/2}$, and one can rewrite Eq. (B6) as follows:

$$\varphi_k^{\text{eff}} = \frac{\varphi_k^{(0)}}{1 + d(1 - (\lambda/64\tilde{N}_e)^{1/2})}. \tag{B7}$$

From Eq. (B7) it is evident that the compensation effect by the loops is not full, as long as the loops placed on the chain are shorter than its entanglement length (nontopological loops) $\lambda < \tilde{N}_e$. This compensation can be accounted for as an effective decrease of the loop fraction parameter to $d_{\text{eff}} < d$, such that

$$1 - \frac{d_{\text{eff}}}{d} = \left(\frac{\lambda}{64\tilde{N}_e}\right)^{1/2} < 1. \tag{B8}$$

Then, the increase of entanglement length of a chain folded into loops can be described as a result of backbone shortening of a chain with the effective loop fraction parameter d_{eff}:

$$\varphi_k^{\text{eff}} = \frac{\varphi_k^{(0)}}{1 + d_{\text{eff}}}. \tag{B9}$$

Indeed, for sufficiently short loop sizes $\lambda < \lambda_{cr} = 64\tilde{N}_e$, the loops induce the decrease of the effective entanglement density and the associated increase of the entanglement length N_e of the backbone. At λ_{cr}, the loops are not Gaussian anymore, violating the condition of unentangled loops and, thus, ceasing the dilution of entanglements in the system.

APPENDIX C: POLYMER SIMULATIONS

Polymer simulations are done using POLYCHROM [61], a wrapper around the open-source GPU-assisted molecular-dynamics package OPENMM [62]. In simulations of crumpled polymers with loops the polymer is represented as a closed unknotted chain (ring) of $N \approx 90\,000$ monomers with one monomer corresponding to 1 kb, so that the total simulated genomic length is 90 Mb. The chains are equipped with harmonic bonds U_{bond}, quadratic angular potential U_{angle}, and excluded volume U_{EV} interactions. Simulations are conducted in the box with periodic boundary conditions (PBC) at volume density $\rho\sigma^3 \approx 0.3$.

The excluded volume potential U_{EV} is introduced via the auxiliary Weeks-Chandler-Anderson (WCA) potential $U(r_i, r_j)$ [63,64], which is a lifted Lennard-Jones repulsive branch

$$U(r_{ij} = |\mathbf{r_i} - \mathbf{r_j}|) = \begin{cases} 4\varepsilon((\sigma/r_{ij})^{12} - (\sigma/r_{ij})^6) + \varepsilon, & r_{ij} \le 2^{1/6}\sigma, \\ 0, & r_{ij} > 2^{1/6}\sigma, \end{cases} \tag{C1}$$

where $\sigma = 0.02$ μm is the characteristic scale of the excluded volume repulsion and $\varepsilon = 1$. In order to avoid strong repulsive forces close to the singularity of Eq. (C1) in simulations, the WCA potential is further smoothly truncated

$$U_{\text{ev}}(r_{ij}) = \mathcal{H}(U(r_{ij}) - \varepsilon_{tr}0)\varepsilon_{\text{tr}}\left(1 + \tanh\left[\frac{U(r_{ij})}{\varepsilon_{tr}} - 1\right]\right) + \mathcal{H}(\varepsilon_{\text{tr}} - U(r_{ij}))U(r_{ij}), \tag{C2}$$

at the prescribed truncation value $\varepsilon_{\text{tr}} = 10$ corresponding to a strong mutual volume exclusion of the beads. In Eq. (C2) $\mathcal{H}$ is the step function. The potential Eq. (C2) acts between every pair of beads, except for neighboring ones.

The energy of harmonic bonds reads as follows:

$$U_{\text{bond}} = \frac{3}{2a^2}\sum_{i=1}^{N-1}(r_{i,i+1} - l_b)^2, \tag{C3}$$

where a is the standard deviation of the monomer-to-monomer distance $r_{i,i+1} = |\mathbf{r_{i+1}} - \mathbf{r_i}|$ from the equilibrium bond length l_b. We set $a \approx 0.06\sigma$. In order to repress occasional crossing of two closely located polymer bonds one through another, we choose the value of the equilibrium bond length $l_b = 0.8\sigma$. Decreasing the bond length combined with a high excluded volume results in an increase of the energy cost for chain crossing [48,65]. As we find, at volume density $\rho\sigma^3 \approx 0.3$ the decrease of l_b by 20% compared to the excluded volume scale σ ensures the loops do not get catenated in the course of extrusion and further equilibration. At larger values of l_b some of the loops become occasionally catenated. The catenations between the fixed loops are detected by computing the matrices of pairwise linking numbers at different times of the simulation as done in Ref. [66].

The angular energy is a harmonic quadratic potential for the consecutive bond angles $\theta_{i,i+1,i+2}$ between the corresponding monomers:

$$U_{\text{angle}} = \sum_{i=1}^{N-2} k(\theta_{i,i+1,i+2} - \theta_0)^2. \tag{C4}$$

We choose $k = 2$ and $\theta_0 = \pi$. The resulting persistence length of such a model is found to be $l_p = 1.75$ monomers and the Kuhn segment $l_k = 3.5$.

In order to test if compartments can interfere with loop extrusion and change the resulting $P(s)$, we also introduce block-copolymer interactions in some of our simulations. Annotation into A and B compartments for simulations is taken from Hi-C experiments (the first eigenvector of the centralized observed over expected Hi-C map; chromosome 14 in 250-kb resolution [67], HeLa cell line). The resulting median size of the compartmental domains is approximately 2.3 Mb. The attractive potential between the beads of the same type is the same as described in Ref. [66].

First, the ring chain without loops is equilibrated in the PBC box starting from a knot-free configuration. After the equilibration, the averaged contact probability resembles a typical law for the unknotted nonconcatenated rings with $(d\log P(s)/d\log s) \approx -1.1$ (Supplemental Material Fig. S7A [44]).

At the second step, we gradually extrude (one side) the loops on the chain and then fix the loops positions. Extrusion is chosen instead of the instantaneous fixation of the loops in their final positions in order to make sure that the loops are not catenated with each other. We check explicitly that the loops are indeed noncatenated at the end of the extrusion by computing the Gaussian linking number for each pair of the loops [66]. Loops constraints are introduced as additional harmonic bonds between nonneighboring beads of the same energy as the polymer bonds Eq. (C3). The loop lengths $l_1, l_2, \ldots, l_k$, $k = [N/(\lambda + g)]$ are drawn randomly from the exponential distribution with the mean $\lambda = 100$ kb. The starting positions of the loop extruders $x_1, x_2, \ldots, x_k$ are drawn randomly, such that the gap lengths $x_{i+1} - x_i - l_i$ for $i = 1, 2, \ldots, k-1$ are distributed exponentially with the mean g. We extrude the loops up to the precalculated lengths and then equilibrate

the chain with fixed extruders at their final positions for another diffusive relaxation time.

To ensure the chain with loops is sufficiently equilibrated, we compute the displacement of a single monomer in the frame of the center of mass of the chain (g_2 function in notations [68]) in the course of simulation. As we show in Supplemental Material Fig. S7C [44], at some point the displacements saturate at the gyration size of the whole chain. At this point, the monomer starts displacing together with the center of mass of the chain (diffusive relaxation time), which is dynamic evidence of sufficient equilibration of the chain. To provide an estimate of the computation time, such a simulation takes approximately ten days on a single GPU core (NVidia RTX 2080 Ti).

We also look into the dynamics of the chains with and without loops at equilibrium (Supplemental Material Fig. S7D [44]). For that, we compute the mean-squared displacements of monomers after sufficient equilibration of the chains (see above) is performed. The times are calibrated in both plots in Figs. S7C and S7D of the Supplemental Material [44] to match the Rouse diffusion coefficient $D_R \approx 0.005\ \mu m^2\ s^{-1/2}$ [54]. Interestingly, we observe that the typical monomer displacements are rather weakly sensitive to the fraction of fixed loops on the chain. At several seconds, there is a crossover from ballistic to Rouse behavior with $\mathrm{MSD}(t) \sim t^{1/2}$, followed by the crossover at $t \sim 10^2$–10^3 to $\mathrm{MSD}(t) \sim t^{1/3}$, which propagates until the relaxation time of the chain; Supplemental Material Fig. S7C [44]. The $1/3$ exponent is close to the theoretical results of the self-consistent fractal loopy globule (0.29) [3], annealed lattice animal model (0.26) [69], as well as to the Gaussian or generalized Rouse prediction (0.4) [4,6]; it was reported before in simulations of crumpled rings as well [3,68]. Another one $(1/2)$ is the Rouse exponent, which characterizes dynamics of chains at scales where they effectively behave as ideal and unentangled [12,32]. Accordingly, the crossover from unentangled to entangled dynamics happens at displacements of the same order of magnitude (approximately $0.1\ \mu m^2$) as the squared gyration size of the chain backbone of length $N_e(\lambda/g)$.

Quantitative analyses of the chains from simulations are conducted using the module for the analyses of polymer conformations in POLYCHROM (polymer_analyses). The contact probability is computed for two cutoff radii, cutoff $= 3\sigma$ and 5σ.

To calculate the entanglement length of the backbones in our simulations, we generalize the expression for the end-to-end squared distance $R^2(s)$ in the wormlike chain model to account for the crossover at N_e. Specifically, we consider the following model:

$$R^2(s|N_e) = \begin{cases} R^2_{\mathrm{WLC}}(s) & \text{for } s \le N_e, \\ (s/N_e)^{2/3} R^2_{\mathrm{WLC}}(N_e) & \text{for } s > N_e, \end{cases} \tag{C5}$$

which is further smoothed using the exponential distribution of N_e,

$$R^2(s) = \frac{1}{N_e} \int_0^\infty R^2(s|N'_e) \exp(-N'_e/N_e) dN'_e. \tag{C6}$$

The functional form of $R^2_{\mathrm{WLC}}(s)$ accounts for the transition from the rodlike behavior at short scales to the random-walk behavior at larger scales describing a persistent polymer chain [51]

$$R^2_{\mathrm{WLC}}(s) = 2 l_p s \left(1 - \frac{l_p}{s}(1 - \exp[-s/l_p])\right). \tag{C7}$$

The integration Eq. (C6) is performed numerically for various pairs of parameters l_p and N_e with the steps $\Delta l_p = 0.25$ and $\Delta N_e = 10$. The obtained curves are fit to the end-to-end distances computed on the simulated backbone trajectories in the interval [0, 1000] monomers (1 Mb); see Figs. S4–S6 in the Supplemental Material [44]. The error of the fit ε_0 is computed as the pointwise L_2 distance between theoretical and numerical curves (mean-squared error). The optimal set of (l_p, N_e) values is determined as the pair yielding the minimum value of the error ε_0. An error of optimal N_e is estimated as the interval around the optimal value yielding the error of fit not exceeding 150% of ε_0.

APPENDIX D: ESTIMATION OF THE CRITICAL EQUILIBRIUM LOOP EXTRUSION SCALE

The fixed loops model is a reasonable approximation of the active loop extrusion process at scales, for which the extrusion rate $r_{\mathrm{coh}} \approx 1$ kb/s is smaller than the rate of thermal relaxation. In contrast with the rate of active extrusion, the passive relaxation rate of a polymer nonlinearly depends on the contour (genomic) length scale, s; e.g., in the framework of the Rouse model, it can be estimated as $r_{\mathrm{th}} = s/\tau_R(s) = l_K^2/(\tau_0 s)$, where τ_0 is the microscopic Rouse time (the diffusion time of one monomer at the scale of order of the Kuhn length [12,51,70]). Thus, at short length scales $s < s^*$, thermal relaxation is faster than extrusion and the chain is effectively at equilibrium, while at larger scales $s > s^*$, the nonequilibrium effects should be important. The crossover scale between the two regimes is

$$s^* = l_k^2 (r_{\mathrm{coh}} \tau_0)^{-1}. \tag{D1}$$

The reported microscopic parameters for chromatin in the literature vary greatly and are quite ambiguous [71,72]. For the coarse-grained modeling one typically takes $l_k = 3 \div 4$ kb, [73,74]; the reference value of the Rouse diffusion coefficient is $D_R \sim 10^{-2}\ \mu m^2\ s^{-1/2}$ [54,73]. This yields $\tau_0 = r_k^4 D_R^{-2} \approx 10^{-1} \div 10^{-2}$ s for the Rouse microscopic time, where we use the conversion ratio $c = 60$ bp/nm and the Kuhn segment size $r_k \approx 50$ nm.

Note, however, that a small uncertainty of approximately 10 nm (20%) in the Kuhn segment size translates into an order of magnitude uncertainty for the microscopic Rouse time.

Plugging these values into Eq. (D1), one arrives at the following rough estimate of the crossover genomic scale:

$$s^* \approx 100 - 1000 \text{ kb}. \tag{D2}$$

[1] J. D. Halverson, J. Smrek, K. Kremer, and A. Y. Grosberg, *From a melt of rings to chromosome territories: The role of topological constraints in genome folding*, Rep. Prog. Phys. **77**, 022601 (2014).

[2] K. Polovnikov, S. Nechaev, and M. V. Tamm, *Effective Hamiltonian of topologically stabilized polymer states*, Soft Matter **14**, 6561 (2018).

[3] T. Ge, S. Panyukov, and M. Rubinstein, *Self-similar conformations and dynamics in entangled melts and solutions of nonconcatenated ring polymers*, Macromolecules **49**, 708 (2016).

[4] K. E. Polovnikov, M. Gherardi, M. Cosentino-Lagomarsino, and M. V. Tamm, *Fractal folding and medium viscoelasticity contribute jointly to chromosome dynamics*, Phys. Rev. Lett. **120**, 088101 (2018).

[5] A. Rosa and R. Everaers, *Structure and dynamics of interphase chromosomes*, PLoS Comput. Biol. **4**, e1000153 (2008).

[6] M. V. Tamm, L. I. Nazarov, A. A. Gavrilov, and A. V. Chertovich, *Anomalous diffusion in fractal globules*, Phys. Rev. Lett. **114**, 178102 (2015).

[7] J. F. Marko, *Micromechanical studies of mitotic chromosomes*, Chromosome research : an international Journal on the molecular, supramolecular and evolutionary aspects of chromosome biology **16**, 469 (2008).

[8] D. Saintillan, M. Shelley, and A. Zidovska, *Extensile motor activity drives coherent motions in a model of interphase chromatin*, Proc. Natl. Acad. Sci. U.S.A. **115**, 11442 (2018).

[9] R. Bruinsma, A. Y. Grosberg, Y. Rabin, and A. Zidovska, *Chromatin hydrodynamics*, Biophys. J. **106**, 1871 (2014).

[10] E. Lieberman-Aiden *et al.*, *Comprehensive mapping of long-range interactions reveals folding principles of the human genome*, Science **326**, 289 (2009).

[11] L. Mirny and J. Dekker, *Mechanisms of chromosome folding and nuclear organization: Their interplay and open questions*, Cold Spring Harbor Perspect. Biol. **14**, a040147 (2022).

[12] A. Y. Grosberg and A. R. Khokhlov, *Statistical Mechanics of Macromolecules* (AIP, Woodbury, NY, 1994), p. 350.

[13] L. Mirny, *The fractal globule as a model of chromatin architecture in the cell*, Chromosome Res. **19**, 37 (2011).

[14] A. Grosberg, S. Nechaev, and E. Shakhnovich, *The role of topological constraints in the kinetics of collapse of macromolecules*, J. Phys. (Paris) **49**, 2095 (1988).

[15] A. Grosberg, Y. Rabin, S. Havlin, and A. Neer, *Crumpled globule model of the three-dimensional structure of DNA*, Europhys. Lett. **23**, 373 (1993).

[16] A. Grosberg, *Annealed lattice animal model and Flory theory for the melt of non-concatenated rings: Towards the physics of crumpling*, Soft Matter **10**, 560 (2014).

[17] A. Rosa and R. Everaers, *Ring polymers in the melt state: The physics of crumpling*, Phys. Rev. Lett. **112**, 118302 (2014).

[18] J. D. Halverson, W. B. Lee, G. S. Grest, A. Y. Grosberg, and K. Kremer, *Molecular dynamics simulation study of nonconcatenated ring polymers in a melt. I. Statics*, J. Chem. Phys. **134**, 204904 (2011).

[19] G. Fudenberg, N. Abdennur, M. Imakaev, A. Goloborodko, and L. Mirny, *Emerging evidence of chromosome folding by loop extrusion*, Cold Spring Harbor Symp. Quant. Biol. **82**, 45 (2017).

[20] A. Goloborodko, J. F. Marko, and L. A. Mirny, *Chromosome compaction by active loop extrusion*, Biophys. J. **110**, 2162 (2016).

[21] M. Ganji, I. A. Shaltiel, S. Bisht, E. Kim, A. Kalichava, C. H. Haering, and C. Dekker, *Real-time imaging of DNA loop extrusion by condensin*, Science **360**, 102 (2018).

[22] R. K. Sachs, G. Van Den Engh, B. Trask, H. Yokota, and J. E. Hearst, *A random-walk/giant-loop model for interphase chromosomes*, Proc. Natl. Acad. Sci. U.S.A. **92**, 2710 (1995).

[23] M. Bohn, D. W. Heermann, and R. van Driel, *Random loop model for long polymers*, Phys. Rev. E **76**, 051805 (2007).

[24] J. Mateos-Langerak *et al.*, *Spatially confined folding of chromatin in the interphase nucleus*, Proc. Natl. Acad. Sci. U.S.A. **106**, 3812 (2009).

[25] C. Münkel, R. Eils, S. Dietzel, D. Zink, C. Mehring, G. Wedemann, T. Cremer, and J. Langowski, *Compartmentalization of interphase chromosomes observed in simulation and experiment*, J. Mol. Biol. **285**, 1053 (1999).

[26] O. Shukron and D. Holcman, *Statistics of randomly cross-linked polymer models to interpret chromatin conformation capture data*, Phys. Rev. E **96**, 012503 (2017).

[27] S. Brahmachari and J. F. Marko, *Chromosome disentanglement driven via optimal compaction of loop-extruded brush structures*, Proc. Natl. Acad. Sci. U.S.A. **116**, 24956 (2019).

[28] M. Barbieri, M. Chotalia, J. Fraser, L.-M. Lavitas, J. Dostie, A. Pombo, and M. Nicodemi, *Complexity of chromatin folding is captured by the strings and binders switch model*, Proc. Natl. Acad. Sci. U.S.A. **109**, 16173 (2012).

[29] O. Shukron and D. Holcman, *Transient chromatin properties revealed by polymer models and stochastic simulations constructed from chromosomal capture data*, PLoS Comput. Biol. **13**, e1005469 (2017).

[30] T.-H. S. Hsieh *et al.*, *Enhancer-promoter interactions and transcription are largely maintained upon acute loss of CTCF, cohesin, WAPL or YY1*, Nat. Genet. **54**, 1919 (2022).

[31] S. Rao *et al.*, *Cohesin loss eliminates all loop domains*, Cell **171**, 305 (2017).

[32] M. Rubinstein and R. Colby, *Polymer Physics* (Oxford University Press, Oxford, 2003).

[33] P. G. De Gennes, *Scaling Concepts in Polymer Physics*, (Cornell University Press, Ithaca, 1979).

[34] A. Rosa and R. Everaers, *Beyond flory theory: Distribution functions for interacting lattice trees*, Phys. Rev. E **95**, 012117 (2017).

[35] K. E. Polovnikov, S. Nechaev, and M. V. Tamm, *Many-body contacts in fractal polymer chains and fractional Brownian trajectories*, Phys. Rev. E **99**, 032501 (2019).

[36] B. Pradhan *et al.*, *SMC complexes can traverse physical roadblocks bigger than their ring size*, Cell Rep. **41**, 111491 (2022).

[37] S. Rao *et al.*, *A 3D map of the human genome at kilobase resolution reveals principles of chromatin looping*, Cell **159**, 1665 (2014).

[38] N. Krietenstein *et al.*, *Ultrastructural details of mammalian chromosome architecture*, Mol. Cell **78**, 554 (2020).

[39] B. Akgol Oksuz *et al.*, *Systematic evaluation of chromosome conformation capture assays*, Nat. Methods **18**, 1046 (2021).

[40] A. Tedeschi *et al.*, *Wapl is an essential regulator of chromatin structure and chromosome segregation*, Nature (London) **501**, 564 (2013).

[41] P. Pedler, *Occupation times for two-state Markov chains*, J. Appl. Probab. **8**, 381 (1971).

[42] The linear loop fraction (i.e., the mean fraction of the chain folded into loops) is approximately $\lambda/(\lambda+g)=(1+d^{-1})^{-1}$. In the limit of sparse loops $d \ll 1$, the loop fraction coincides numerically with d. In general, the growth of the fraction parameter d is related to the growth of the loop fraction. Therefore, we use them interchangeably in the text when referring to qualitative changes.

[43] W. Schwarzer *et al.*, *Two independent modes of chromatin organization revealed by cohesin removal*, Nature (London) **551**, 51 (2017).

[44] See Supplemental Material at http://link.aps.org/supplemental/10.1103/PhysRevX.13.041029 for the full expressions of the contact probabilities corresponding to different diagrams and Supplemental Figures.

[45] S. Nechaev, A. Semenov, and M. Koleva, *Dynamics of a polymer chain in an array of obstacles*, Physica (Amsterdam) **140A**, 506 (1987).

[46] J. D. Halverson, G. S. Grest, A. Y. Grosberg, and K. Kremer, *Rheology of ring polymer melts: From linear contaminants to ring-linear blends*, Phys. Rev. Lett. **108**, 038301 (2011).

[47] N. Uchida, G. Grest, and R. Everaers, *Viscoelasticity and primitive path analysis of entangled polymer liquids: From F-actin to polyethylene*, J. Chem. Phys. **128**, 044902 (2008).

[48] R. Everaers, S. K. Sukumaran, G. S. Grest, C. Svaneborg, A. Sivasubramanian, and K. Kremer, *Rheology and microscopic topology of entangled polymeric liquids*, Science **303**, 823 (2004).

[49] A. R. Khokhlov and S. K. Nechaev, *Polymer chain in an array of obstacles*, Phys. Lett. **112A**, 156 (1985).

[50] M. Rubinstein, *Dynamics of Ring polymers in the presence of fixed obstacles*, Phys. Rev. Lett. **57**, 3023 (1986).

[51] M. Doi and S. Edwards, *The Theory of Polymer Dynamics* (Oxford University Press, Oxford, 1988).

[52] S. Ghosh and D. Jost, *How epigenome drives chromatin folding and dynamics, insights from efficient coarse-grained models of chromosomes*, PLoS Comput. Biol. **14**, e1006159 (2018).

[53] A. Hafner, M. Park, S. Berger, E. Nora, and A. Boettiger, *Loop stacking organizes genome folding from TADs to chromosomes*, Mol. Cell **83**, 1377 (2023).

[54] M. Gabriele, H. B. Brandão, S. Grosse-Holz, A. Jha, G. M. Dailey, C. Cattoglio, T.-H. S. Hsieh, L. Mirny, C. Zechner, and A. S. Hansen, *Dynamics of CTCF- and cohesin-mediated chromatin looping revealed by live-cell imaging*, Science **376**, 496 (2022).

[55] B. Bintu, L. J. Mateo, J.-H. Su, N. A. Sinnott-Armstrong, M. Parker, S. Kinrot, K. Yamaya, A. N. Boettiger, and X. Zhuang, *Super-resolution chromatin tracing reveals domains and cooperative interactions in single cells*, Science **362**, eaau1783 (2018).

[56] E. J. Banigan and L. Mirny, *Loop extrusion: Theory meets single-molecule experiments*, Curr. Opin. Cell Biol. **64**, 124 (2020).

[57] J. Gibcus *et al.*, *A pathway for mitotic chromosome formation*, Science **359**, 2133 (2018).

[58] S. A. Schalbetter, G. Fudenberg, J. Baxter, K. S. Pollard, and M. J. Neale, *Principles of meiotic chromosome assembly revealed in S. Cerevisiae*, Nat. Commun. **10**, 1 (2019).

[59] J. Paturej, S. S. Sheiko, S. Panyukov, and M. Rubinstein, *Molecular structure of bottle-brush polymers in melts*, Sci. Adv. **2**, e1601478 (2016).

[60] M. Abramowitz, I. A. Stegun, and R. H. Romer, *Handbook of Mathematical Functions with Formulas, Graphs, and Mathematical Tables* (U.S. GPO, Washington, DC, 1964), Vol. 55.

[61] https://github.com/open2c/polychrom.

[62] P. Eastman and V. Pande, *OPENMM: A hardware-independent framework for molecular simulations*, Comput. Sci. Eng. **12**, 34 (2010).

[63] J. Weeks, D. Chandler, and H. Anderson, *Role of repulsive forces in determining the equilibrium structure of simple liquids*, J. Chem. Phys. **54**, 5237 (1971).

[64] K. Kremer and G. Grest, *Dynamics of entangled linear polymer melts: A moleculardynamics simulation*, J. Chem. Phys. **92**, 5057 (1990).

[65] R. Auhl, R. Everaers, G. S. Grest, K. Kremer, and S. J. Plimpton, *Equilibration of long chain polymer melts in computer simulations*, J. Chem. Phys. **119**, 12718 (2003).

[66] E. Hildebrand *et al.*, *Chromosome decompaction and cohesin direct topoisomerase II activity to establish and maintain an unentangled interphase genome*, bioRxiv.

[67] K. Abramo, A.-L. Valton, S. V. Venev, H. Ozadam, A. Nicole Fox, and J. Dekker, *A chromosome folding intermediate at the condensin-to-cohesin transition during telophase*, Nat. Cell Biol. **21**, 1393 (2019).

[68] J. D. Halverson, W. B. Lee, G. S. Grest, A. Y. Grosberg, and K. Kremer, *Molecular dynamics simulation study of nonconcatenated ring polymers in a melt. II. Dynamics*, J. Chem. Phys. **134**, 204905 (2011).

[69] J. Smrek and A. Grosberg, *Understanding the dynamics of rings in the melt in terms of the annealed tree model*, J. Phys. Condens. Matter **27**, 064117 (2015).

[70] M. V. Tamm and K. Polovnikov, *Dynamics of Polymers: Classic Results and Recent Developments. Order, Disorder and Criticality: Advanced Problems of Phase Transition Theory* (World Scientific, Singapore, 2018).

[71] J. Dekker, K. Rippe, M. Dekker, and K. N., *Capturing chromosome conformation*, Science **295**, 1306 (2002).

[72] K. Bystricky, P. Heun, L. Gehlen, J. Langowski, and S. M. Gasser, *Long-range compaction and flexibility of*

interphase chromatin in budding yeast analyzed by high-resolution imaging techniques, Proc. Natl. Acad. Sci. U.S.A. **101**, 16495 (2004).

[73] J. Nuebler, S. Holzer, L. Pellegrini, and S. D. Bell, *Chromatin organization by an interplay of loop extrusion and compartmental segregation*, Proc. Natl. Acad. Sci. U.S.A. **115**, 6697 (2018).

[74] M. M. Tortora, H. Salari, and D. Jost, *Chromosome dynamics during interphase: A biophysical perspective*, Curr. Opin. Genet. Dev. **61**, 37 (2020).